SEDIMENTOLOGY the journal of the International Association of Sedimentologists IAS

Sedimentology (2026) doi: 10.1111/sed.70085

Response of unconfined turbidity currents orthogonally to en-echelon segmented folds: Insights from numerical modelling

HONGXIANG XU*,†,‡, ZHIYUAN GE*,†,‡, ROB L. GAWTHORPE§ and DANIELLE M. HOWLETT¶

**Hainan Institute of China University of Petroleum (Beijing), Sanya 572025, China (E-mail: gezhiyuan@cup.edu.cn)*

†State Key Laboratory of Petroleum Resources and Engineering, China University of Petroleum (Beijing), Beijing 102249, China

‡College of Geosciences, China University of Petroleum (Beijing), Beijing 102249, China

§Department of Earth Science, University of Bergen, 5007, Bergen, Norway

¶Vår Energi ASA, 4313, Sandnes, Norway

Associate Editor: Fabrizzio Felleti

ABSTRACT

Deep-water fold and thrust belts (DWFTBs) exert a first-order control on turbidity current dynamics and sediment dispersal, yet the influence of segmented folds on flow behaviour and resultant deposition remains poorly constrained. This study integrates structural modelling and computational fluid dynamics (CFD) to investigate the hydraulic behaviour and depositional patterns of unconfined turbidity currents interacting with en-echelon segmented folds. Upon encountering segmented folds, unconfined turbidity currents decelerate and thicken due to reverse underflow and overflow, generating low-frequency hydraulic jumps with low-amplitude fluctuations of Froude number (*Fr*) and height-suppressed Kelvin–Helmholtz (K–H) waves upstream of folds. Concurrently, volumetrically small and dilute currents spill through fold segment boundaries, forming high-frequency hydraulic jumps with high-amplitude fluctuations of *Fr* and enhanced K–H waves downstream of folds. Upstream hydraulic jumps dominate the preferential sediment deposition into three distinct depozones: (i) strike-parallel depozones upslope of backlimbs from reverse overflow, (ii) strike-parallel elliptical depozones along the base of fold backlimbs from reverse underflow and overflow and (iii) localised transverse depozones on fold backlimbs from waning overspill. The influence of segmented folds on overrunning currents is determined by segment boundary relief, governed by across-strike distance (*AcD*) and evolutionary stages. En-echelon folds with low linkage ratios at early stage of linkage facilitate flow transfer through low-relief segment boundaries. At late-stage of linkage, sediment transport across folds depends on *AcD*: large *AcD* maintains a flow pathway through the segment boundary, whereas small *AcD* blocks flow. As en-echelon folds evolve, reduced along-strike distance (*AlD*) diminishes sediment deposition. The depocentre migrates from the base of upslope fold backlimb to that of downslope fold as *AcD* decreases. Since en-echelon segmented folds are common features in DWFTBs, and in salt- or shale-influenced basins, these findings highlight the critical role of segmented boundaries and their linkage processes in controlling turbidity current hydrodynamics and turbiditic sedimentation.

Keywords Deep-water fold and thrust belt, hydraulic jump, numerical modelling, sand dispersal, segmented fold, turbidity currents.

INTRODUCTION

Turbidity currents, serving as the dominant process of sediment transport on continental margins, ultimately constructing most extensive submarine depositional systems on Earth (Galy *et al.*, 2007; Meiburg & Kneller, 2010; Talling *et al.*, 2012; Kane *et al.*, 2020; Pope *et al.*, 2022a). In tectonically active basins, structurally controlled topography exerts first-order controls on the hydraulics and depositional characteristics of turbidity currents (Ravnås & Steel, 1998; Gawthorpe & Leeder, 2000; Gee & Gawthorpe, 2006; Mayall *et al.*, 2010). Within deep-water fold-thrust belts (DWFTBs), the syndepositional growth of compressional structures generates intricate three-dimensional seafloor morphologies through fold segment interaction and progressive structural evolution (Pizzi *et al.*, 2020). This structural topography triggers critical hydraulic transitions as supercritical flows interact with fold backlimb counter-slopes, characterised by flow deceleration and vertical thickening that culminates in hydraulic jumps (Pantin & Leeder, 1987; Alexander & Morris, 1994; Tinterri, 2025). These hydraulic phenomena emerge through a dual reverse flow mechanism: a surface overflow generated through flow self-reflection processes, and a basal underflow resulting from backward extrusion of the dense near-bed sediment-laden layer (Patacci *et al.*, 2015; Tinterri *et al.*, 2016; Howlett *et al.*, 2019). Meanwhile, certain turbidity currents either surmount the fold crest or divert along its flanks, subsequently continuing their downslope spread along the forelimb (Clark & Cartwright, 2009, 2011; Howlett *et al.*, 2021). These processes ultimately govern the locations, geometries and facies of individual depositional elements, and the basin-scale distribution of deep-water sedimentary systems (Gee *et al.*, 2007; Oluboyo *et al.*, 2014; Tinterri & Piazza, 2019; Don *et al.*, 2020; McArthur *et al.*, 2022).

Lateral linkage during progressive fold segment growth is a key aspect in the evolution of DWFTBs, as demonstrated through integrated observational and modelling approaches (Grujić, 1993; Johns & Mosher, 1996; Schmid *et al.*, 2008). Three-dimensional finite element modelling by Grasemann & Schmalholz (2012) identifies four distinct structural configurations between adjacent fold segments: (i) linear linkage, (ii) oblique linkage, (iii) oblique non-linkage

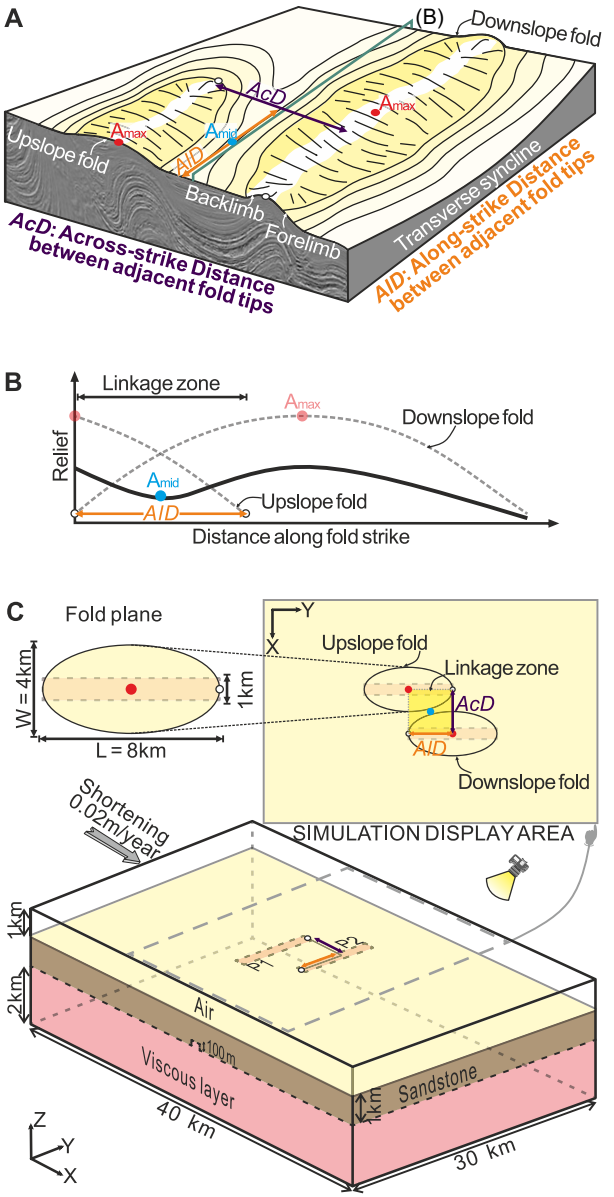

Fig. 1. Segmented fold topography and structural model design. (A) Block diagram of segmented fold topography with the definitions of across-strike distance (*AcD*) and along-strike distance (*AlD*) (seismic cross-section slightly modified from https://www.pgs.com/data-library/hotspots/malaysia/geology). (B) Schematic relief profile corresponding to the topography in (A), with explanation of the structural terminology used in this study (based partly on Ramsey *et al.*, 2008; Grasemann & Schmalholz, 2012). (C) Schematic diagram (not drawn to scale) of the structural model used in this study. The middle half of the sandstone top surface was imported into turbidity currents modelling as the segmented fold topography. For visualisation purposes, the Z axis has been exaggerated tenfold.

and (iv) linear non-linkage. Research on turbidite sedimentation around growth folds primarily addresses two aspects: (1) hydrodynamic interactions between turbidity currents and individual fold topography (e.g. flow reflection, deflection and hydraulic jump) through outcrops and flume tank simulations (Kneller *et al.*, 1991; Kneller, 1995; Kneller & McCaffrey, 1995, 1999; Morris & Alexander, 2003; Amy *et al.*, 2004; Tinterri & Tagliaferri, 2015; Cumberpatch *et al.*, 2021; Keavney *et al.*, 2025), and (2) characteristics of deep-water deposits, such as submarine channel-lobe systems and mass transport complexes reconstructed from seismic facies and seismic geomorphological analysis (Morley & Leong, 2008; Anderson *et al.*, 2013; Doughty-Jones *et al.*, 2017, 2019; Bouchakour *et al.*, 2023). Nevertheless, these studies have some limitations: Outcrop-based reconstructions and seismic interpretations offer only indirect proxies for sedimentation processes, whereas laboratory experiments have the issue of scaling discrepancies in Reynolds and Froude numbers (Wahab *et al.*, 2022). Recent advancements in computational fluid dynamics (CFD) simulations, empowered by expanding databases of in situ monitoring (including velocity profiles, suspended sediment concentrations and thermohaline properties; Hughes Clarke, 2016; Azpiroz-Zabala *et al.*, 2017; Zhang *et al.*, 2018; Heijnen *et al.*, 2022; Muñoz-Royo *et al.*, 2022), have significantly improved the capability to model natural-scale turbidity currents. One strength of CFD modelling is that it enables quantitative analysis of critical hydrodynamic processes, such as reverse underflow generation during flow reflection and Kelvin–Helmholtz wave induced interface destabilisation (Huang *et al.*, 2007, 2012; Abd El-Gawad *et al.*, 2012a,b; Howlett *et al.*, 2019; Salinas *et al.*, 2020, 2021; Ge *et al.*, 2022).

In this contribution, we expand upon the work of Howlett *et al.* (2019) that examined unconfined turbidity currents interactions with solitary fold and isolated co-linear fold segments. We integrate geodynamic process modelling of fault-related folds with CFD simulations to investigate turbidity currents' response to en-echelon segmented folds. We present four experimental scenarios that systematically examine how hydraulic behaviour and sediment dispersal patterns vary as turbidity currents interact with two en-echelon fold segments of different spatial configurations and oblique linkage scenarios.

METHODOLOGY

Segmented fold modelling

Fold segments on continental slopes create complex en-echelon fold networks that affect seafloor topography (Hesse *et al.*, 2009, 2010; Pizzi *et al.*, 2020; McArthur *et al.*, 2022). Individual fold segments exhibit maximum relief at their centres, tapering to zero at their tips, with synclinal depocentres developing between adjacent anticlines (Fig. 1A and B; Nabavi & Fossen, 2021). The spatial and topographic configuration of fold segments in DWFTBs can be described by the across-strike distance (*AcD*) and the along-strike distance (*AlD*) between tips of adjacent fold segments (Fig. 1A). Specifically, the down-slope fold spacing is primarily related to *AcD* (Ramsey *et al.*, 2008; Zhang *et al.*, 2021), whereas lateral spacing and propagation during fold growth are associated with *AlD* (Fernandez & Kaus, 2014a; Song *et al.*, 2021; Gao *et al.*, 2023). A negative *AlD* indicates overlap between two folds.

Segment boundaries are the linkage zones between adjacent fold segments and are local relative topographic lows (Figs 1A and B and 2; Bretis *et al.*, 2011; Grasemann & Schmalholz, 2012; Wu *et al.*, 2020). In this study, we use two parameters to describe the geometry and relief of the linkage zone: the aspect ratio (*AlD*/*AcD*) and the linkage ratio (A_{mid}/A_{max}) (Fig. 1). The aspect ratio is the ratio of *AlD* to *AcD*, similar to the ratio between overlap and separation distance used for linkage between two normal faults (Fig. 1A; Aydin & Schultz, 1990; Long & Imber, 2011; Ge *et al.*, 2018). The fold linkage ratio denotes the ratio of the relative height at the centre of the linkage zone (A_{mid}) to the maximum relative height of fold segment (A_{max}), where relative height is calculated as the surface height minus the mean surface elevation (Figs 1A and B and 2; Grasemann & Schmalholz, 2012). Therefore, a positive linkage ratio (i.e. $A_{mid}/A_{max} > 0$) indicates linkage between fold segments, with values closer to 1 representing strong connectivity. While a negative value (i.e. $A_{mid}/A_{max} < 0$) indicates that two fold segments separate in isolation from each other with non-linkage (Grasemann & Schmalholz, 2012; Collignon *et al.*, 2015).

We utilise Underworld2, an open-source finite element code for geodynamic modelling, to model the three-dimensional fold topography (Moresi *et al.*, 2003; Moresi *et al.*, 2007; https://www.underworldcode.org). It has been validated across multiple scales, from lithospheric

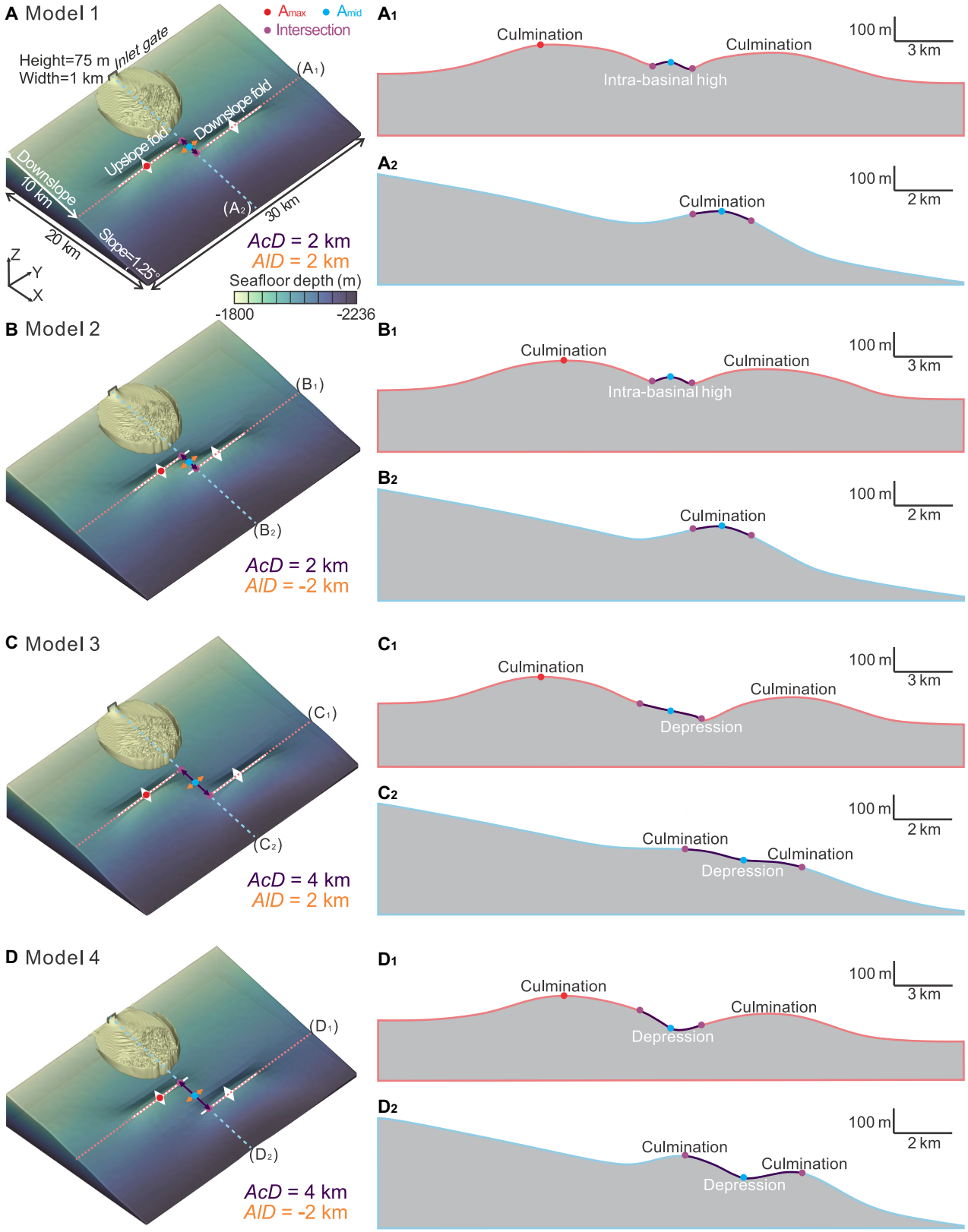

Fig. 2. Segmented fold topography used for turbidity currents simulation in Models 1 to 4 (Table 2). (A–D) Three-dimensional views for (A) Model 1, (B) Model 2, (C) Model 3, and (D) Model 4, with corresponding strike-parallel (A_1–D_1) and strike-orthogonal sections (A_2–D_2) displayed to the right. Note that the positions of A_{max} and A_{mid}, marked with red and blue dots, respectively. The remaining intersections of the associated cross-sections are marked with purple dots. A_{max} is approximately 140 m, and the A_{mid}/A_{max} ratio reflects the relief of the linkage zone. *AcD*, across-strike distance; *AlD*, along-strike distance. The flow was released towards the centre of segmented folds from a 1 km wide and 75 m high inlet gate located 10 km away from the upslope fold. The orange arrow indicates the range of the monitor window for bypassed sediment via linkage zones.

(Huismans & Beaumont, 2011; Moresi *et al.*, 2014) to basin-scale deformation (Cruz *et al.*, 2011; Mondy *et al.*, 2023). Of particular relevance to our study, Underworld2 and other similar FEM codes have successfully resolved key mechanisms controlling fold-thrust belt evolution, including fold nucleation dynamics (Schmalholz, 2008), structural interactions (Fernandez & Kaus, 2014a,b) and their coupling with surface processes (Collignon *et al.*, 2014, 2015).

The model domain spans a three-dimensional space of $40 \times 30 \times 4$ km, comprising $60 \times 45 \times 40$ cells in the X, Y, and Z directions, respectively, with a plan-view resolution of 666 m. Vertically, the model encompasses a 1-km thick stiff sandstone layer overlaying a 2-km thick weak viscous layer. Two step-like perturbations (P1 & P2), identical in material properties to the viscous layer, are prescribed at the interface between sandstone and viscous layer to induce folding at a specific location. Perturbation lengths, widths, and heights are 8 km, 1 km and 100 m, respectively, resulting in fold segment lengths and wavelengths of approximately 8 km and 4 km (Fig. 1C). The material properties of air, sandstone and the viscous layer are represented in Table 1, including densities, effective viscosities, cohesions and angles of internal friction. Two fold segments are subjected to unidirectional compressional stresses to exclude thrust and fold with opposite dip in a DWFTB (Higgins *et al.*, 2007). Boundary conditions are specified as follows: the top side of model ($Z = 4$ km) is free surface (i.e. normal and shear stresses on the surface are zero), while bottom ($Z = 0$ km), front and back ($Y = 0$ and 30 km) associated with right boundaries ($X = 40$ km) are all kept planar with free slip (i.e. $Vz = 0$ or $Vy = 0$ or $Vx = 0$). For the left boundary ($X = 0$ km), a horizontal regional shortening rate of 2 mm year^{-1} (i.e. $Vx = 0.02$ m/year) is applied with each time step of 1000 years (Fig. 1C). The resultant uplift rate at the fold centre is ~3.5 mm year^{-1}, producing a maximum absolute topography of 250 m and a maximum relative height of 150 m after 0.07 Ma (Table 1; Oveisi *et al.*, 2007; Morley, 2009). After the geodynamic simulation, the top sandstone surface is extracted to represent segmented fold topography and superimposed onto a seafloor slope of 1.25°, consistent with the typical regional slopes of DWFTBs that range from 0.8° to 3.0° (Heiniö & Davies, 2006; Jolly *et al.*, 2016). The resultant segmented fold topographies not only represent thrusts fault-related folds in DWFTBs but are also similar to deep-water salt- or shale-cored anticlines (Howlett *et al.*, 2021; Pizzi *et al.*, 2023).

In order to form representative segmented fold topography, values of *AcD* and *AlD* are varied to span critical thresholds in fold network evolution. Increasing *AcD* from 2 km to 4 km represents the across-strike distance between fold segments gradually approaching the critical value of half the fold wavelength with the transition from linkage to non-linkage (Grasemann & Schmalholz, 2012). Decreasing *AlD* from 2 km to −2 km reflects the transition from along-strike separated folds to partially overlapping fold segments. These empirically constrained ranges encompass the majority of natural fold systems documented in global DWFTBs (Morley *et al.*, 2011). Four en-echelon topographic scenarios (Table 2) are selected to assess the potential impact of various segmented fold topography on hydraulic and sedimentological behaviours of unconfined turbidity currents:

1 Model 1 simulates the early-stage of oblique linkage with a small *AcD* of 2 km and *AlD* of 2 km, resulting in a linkage zone aspect ratio of 1. The fold amplitudes ($A_{max} = 140$ m, $A_{mid} = 88$ m) yield a linkage ratio of 0.60 (Fig. 2A, Table 2).

2 Model 2 simulates the late stage of oblique linkage with a small *AcD* of 2 km and *AlD* of

Table 1. Parameters of the natural-scale structural modelling used in this study.

Parameter	Value (model)	Value (prototype)
Length (X)	40 km	40 km
Width (Y)	30 km	30 km
Height (Z)	4 km	4 km
Gravity acceleration	9.81 m s^{-2}	9.81 m s^{-2}
Density (air)	1.2 kg m^{-3}	1.1 to 1.4 kg m^{-3}
Density (sandstone)	2700 kg m^{-3}	1610 to 2760 kg m^{-3} (Manger, 1963)
Density (viscous layer)	2200 kg m^{-3}	2160 to 2200 kg m^{-3} (Jackson & Talbot, 1986)
Effective viscosity (air)	10^{17} Pa s	10^{15} to 10^{18} Pa s
Effective viscosity (sandstone)	10^{22} Pa s	10^{19} to 10^{22} Pa s
Effective viscosity (viscous layer)	10^{19} Pa s	10^{17} to 10^{20} Pa s (Jackson & Hudec, 2017)
Cohesion (sandstone)	10^{7} Pa	10^{7} Pa (Barton & Choubey, 1977)
Cohesion (viscous layer)	8×10^{5} Pa	4×10^{5} to 5×10^{6} Pa (Weijermars *et al.*, 1993)
Angle of internal friction (sandstone)	36°	30° to 40° (Barton & Choubey, 1977)
Angle of internal friction (viscous layer)	22°	20° to 30° (Weijermars *et al.*, 1993)
Angle of internal friction after softening (sandstone)	31°	30° to 40° (Barton & Choubey, 1977)
Angle of internal friction after softening (viscous layer)	21°	20° to 30° (Weijermars *et al.*, 1993)
Time	0.07 Ma	0.07 Ma
Shortening rate	2 mm $year^{-1}$	1 to 10 mm $year^{-1}$ (Oveisi *et al.*, 2007; Simons *et al.*, 2007; Morley, 2009)
Uplift rate	3.36 to 3.70 mm $year^{-1}$	0.3 to 10 mm $year^{-1}$ (Oveisi *et al.*, 2007; Morley, 2009)

Note that the 'Value (model)' column lists the specific parameter values of the natural-scale model, which fall within the typical ranges for prototypes given in the 'Value (prototype)' column.

−2 km (i.e. two fold segments are overlapped with 2 km), resulting in a linkage zone aspect ratio of −1. The fold amplitudes (A_{max} = 150 m, A_{mid} = 118 m) yield a linkage ratio of 0.79 (Fig. 2B, Table 2).

3 Model 3 simulates the early-stage of oblique linkage with a large *AcD* of 4 km and *AlD* of 2 km, resulting in a linkage zone aspect ratio of 0.5. The fold amplitudes (A_{max} = 140 m, A_{mid} = 38 m) yield a linkage ratio of 0.27 (Fig. 2C, Table 2).

4 Model 4 simulates the late stage of oblique linkage with a large *AcD* of 4 km and *AlD* of −2 km, resulting in a linkage zone aspect ratio of −0.5. The fold amplitudes (A_{max} = 129 m, A_{mid} = 18 m) yield a linkage ratio of 0.14 (Fig. 2D, Table 2).

Turbidity currents modelling

FLOW-3D® (see www.flow3d.com) is used for the numerical simulation of three-dimensional unconfined turbidity currents. FLOW-3D® has been thoroughly verified for its reliability through comparisons between physical experiments and numerical simulations of turbidity currents (Heimsund *et al.*, 2007; Basani *et al.*, 2014), and has been extensively applied

Table 2. Four simulation models (Models 1 to 4) were used in this study to assess the influence of various segmented fold configurations with diverse *AcD* and *AlD*.

Simulation model code	Across-strike distance (*AcD*, km)	Along-strike distance (*AlD*, km)	Aspect ratio (*AlD*/*AcD*)	Maximum absolute topography (T_{max}, m)	Minimum absolute topography (T_{min}, m)	Maximum relative height (A_{max}, m)	Minimum relative height (A_{min}, m)	Relative height in horizontal middle of linkage zone (A_{mid}, m)	Linkage ratio (A_{mid}/A_{max})
Model 1	2	2	1	257	79	148	−30	88	0.60
Model 2	2	−2	−1	258	75	150	−34	118	0.79
Model 3	4	2	0.5	256	79	140	−26	38	0.27
Model 4	4	−2	−0.5	237	81	129	−28	18	0.14

to understand the hydraulic and depositional behaviours of turbidity currents over the past decade (Janocko *et al.*, 2013; Ge *et al.*, 2017, 2018; Vellinga *et al.*, 2018; Howlett *et al.*, 2019; Englert *et al.*, 2023). The numerical code describes fluid motion by solving Reynolds-Averaged Navier–Stokes (RANS) equations through finite-difference and finite-volume discretisation on rectangular grids, implementing the $k-\varepsilon$ RNG turbulence model (Yakhot *et al.*, 1992), coupled with fluid–structure interaction and sediment scour models (Flow Science, 2022). The sediment scour model estimates the motion of sediment, that is erosion, advection and deposition by computing the entrainment or settling and suspended or bedload transport of sediments. The Mastbergen & Van Den Berg (2003) formulae are utilised to model sediment entrainment through picking up and re-suspension. Entrainment and settling of sediments are opposite processes that occur concurrently. The Richardson & Zaki (1954) correlation is employed to consider the hindered settling velocity based on suspended sediment concentration and particle Reynolds number, instead of grain-grain interactions in suspension. The Meyer-Peter & Müller (1948) equation is used to model bedload transport of sediment that rolls or bounces over the surface of packed sediment, and the Soulsby–Whitehouse Eq. (1997) predicts the critical Shields parameter based on the angle of repose for inclined surfaces. Further details are available in Ge *et al.* (2017) and the software user manual (Flow Science, 2022).

The experimental set-up adopts hydraulic parameters from Ge *et al.* (2017, 2018) and Howlett *et al.* (2019) to enable comparison of the responses of turbidity currents to different structural topographies, such as solitary folds, normal faults and relay ramps. During the simulation, a uniform sediment-water mixture is released through a 1 km × 75 m inlet gate on a 1.25° slope, sustaining for 2 h as a surge-type turbulent flow (Fig. 2A). The inlet gate is located ca 10 km up dip from segmented fold (Fig. 2A), allowing the flow to self-regulate its initial excess sediment load and stabilise its hydraulic behaviour into quasi-steady currents (Kneller & Branney, 1995) before interacting with the fold topography. Due to low erosional capabilities of unconfined turbidity currents (Middleton, 1993), the substrate is assumed to be non-erodible, but with a surface roughness of fine-grained sand, enabling the flow to erode and re-entrain its

own unconsolidated deposits (Ge *et al.*, 2017; Howlett *et al.*, 2019).

The flow begins with an initial forward velocity of 5 m s^{-1} and a sediment concentration of 8 vol.%. The velocity of natural turbidity currents can vary widely, ranging from <1 m s^{-1} to over 20 m s^{-1}, due to variability in the external triggers and internal hydraulic evolution of the flows (Chikita, 1989; Mulder *et al.*, 1998, 2003; Xu *et al.*, 2004; Talling *et al.*, 2013). Additionally, latest direct monitoring in the Congo Canyon suggests that ~4 to 5 m s^{-1} is the initial frontal velocity threshold for canyon flushing flows (Talling *et al.*, 2022, 2023). In this study, a modest initial velocity of 5 m s^{-1} is assumed to allow the flow to transport sediment while maintaining <15 m s^{-1} velocities across the simulation domain. Depending on the types of flow initiation, the volumetric sediment concentration of natural-scale turbidity currents may range from <0.01 vol.%, entirely dilute and fully turbulent, to up to 80 vol.% with a possible dense near-bed layer (Paull *et al.*, 2018; Wells & Dorrell, 2021; Pope *et al.*, 2022b). The non-cohesive sediment mixture with an initial concentration of 8 vol.%, comprised 25% silt, 50% very fine sand, and 25% fine sand ($\rho = 2.65$ g cm^{-3}), is assumed for the experimental flow to minimise grain-grain interactions while rendering turbulence as the dominant grain-support mechanism (Bagnold, 1954, 1962; Kuenen, 1966; Middleton, 1976; Kessel & Kranenburg, 1996).

The inlet gate scale combined with initial hydraulic parameters mimics a realistic surge-type flow originating from localised mid-slope landslides with various triggering factors such as earthquakes (Lewis, 1971; Piper *et al.*, 1999; Piper & Normark, 2009; Howarth *et al.*, 2021) or from upper-slope large channel, incised valley or shelf canyon with sediment masses supplied by a combination of river floods and tidal flows (Zavala *et al.*, 2006; Talling *et al.*, 2022; Liu *et al.*, 2023). The Reynolds number (*Re*) of the experimental flow is on the order of 10^4 to 10^5, well above the lower limit of 2000 for turbulent flows and in the range of 10^3 to 10^7 generally accepted as large, natural-scale turbidity currents (Middleton, 1993; Meiburg & Kneller, 2010; Cantero *et al.*, 2012; Meiburg *et al.*, 2015).

The 20 × 30 km model domain (−1800 to −2236 m depth range) features adaptive grid resolution (Fig. 2A): 25 to 50 m (X), 50 to 100 m (Y), and 5 m (Z), with post-processing bilinear interpolation achieving 0.05 m vertical resolution for deposition analysis. The 2.6×10^7 cell mesh prioritises refinement in fold interaction zones. Hydraulic parameters are monitored at 60 s intervals, with visualisation outputs including: 0.2 and 0.8 vol.% isoconcentration surfaces, velocity vector fields, ≥10 vol.% sand packing isosurfaces and spatiotemporal heatmaps of depth-averaged Froude number (*Fr*) evolution (Figs 3 to 12). Cross-sectional profiles reveal internal flow structure development. Bypassed sediment flux and cumulative volume are calculated based on flow velocity and sediment concentration monitored within individual cells across the linkage zones (Fig. 13, Table 3). Meanwhile, deposition volumes are quantified through differential bathymetric analysis to characterise sediment distribution patterns (Table 4).

SIMULATION RESULTS

Model 1

The topography in Model 1 comprises two en-echelon fold segments separated by both across-strike (*AcD*) and along-strike distance (*AlD*) of 2 km, and a linkage zone with middle aspect ratio (*AlD*/*AcD* = 1). This combination of structural parameters aims to simulate the early stage of oblique fold linkage involving small *AcD* (<1/2 fold wavelength) (Figs 2A and 3 to 6, Table 2).

Once released from the inlet gate, the turbidity current immediately spread laterally, forming a U-shaped frontal zone (150 to 170 m high) featuring characteristic 'lobe and cleft' structure (Simpson, 1986). Rapid self-regulation through proximal deposition transformed the initial sediment overload into a quasi-steady supercritical flow (Figs 3A, 5A and 6D). Within the first kilometre downstream, flow thickness decreased from 75 m to 50 m while velocity increased from 5 m s^{-1} to 12 m s^{-1}. Flow deceleration initiated 2.5 km downstream through ambient water entrainment, accompanied by thickness increase and bulk concentration reduction below 8 vol.% (Fig. 3A). This process generated large-scale Kelvin–Helmholtz (K–H) waves (200 to 400 m wavelength, 15 to 40 m amplitude) through interfacial shear stress, which induced near-bed velocity fluctuations (6 to 9 m s^{-1}) and concentration variations (4 to 6 vol.%) through vortex development (Figs 3 and 4B).

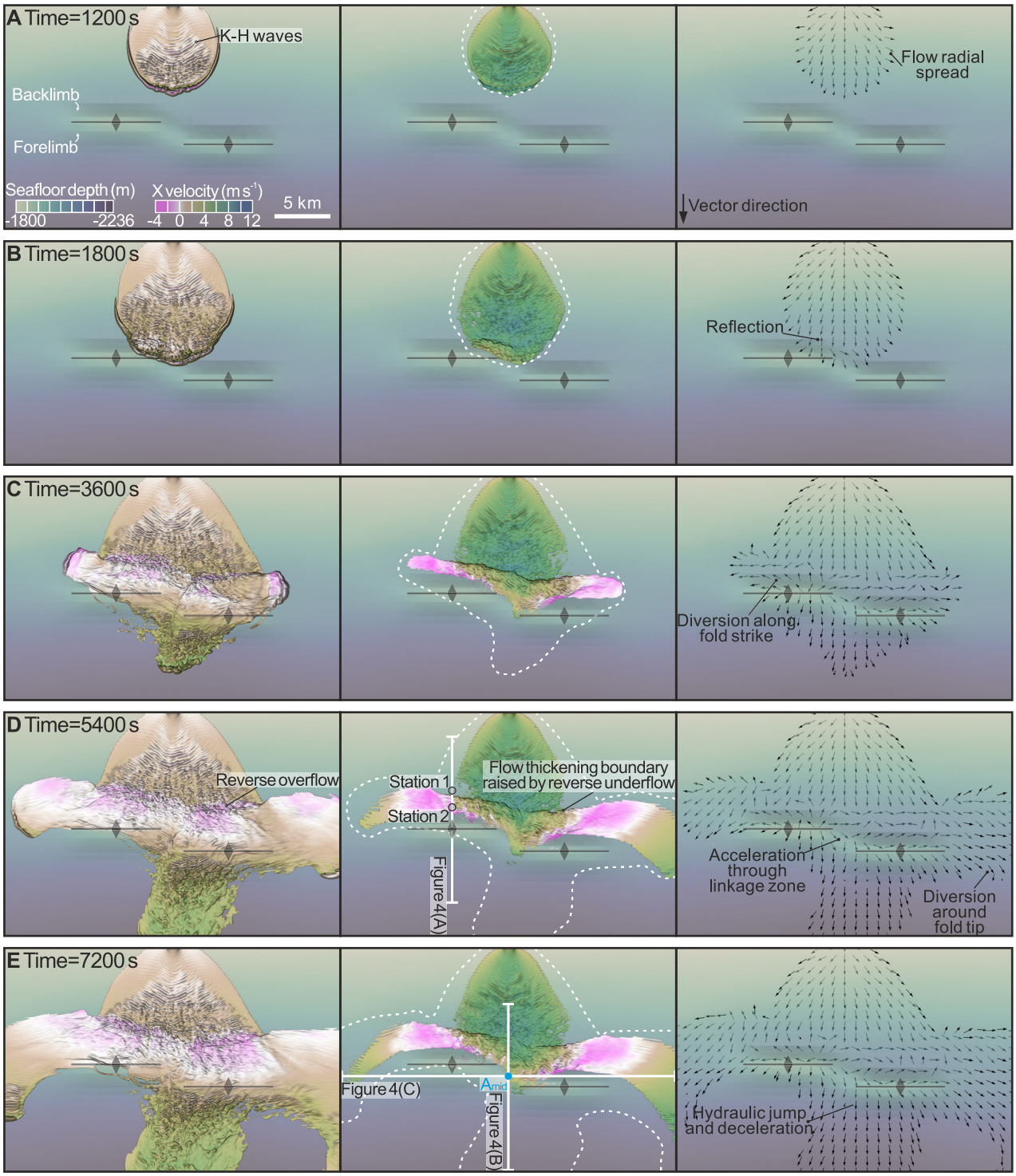

Fig. 3. Hydraulic behaviour of turbidity currents in response to segmented fold in Model 1 (Table 2). (A–E) Plan-view snapshots of the flow sediment isoconcentration surface of 0.2 vol.% (left) and 0.8 vol.% (middle) coloured by X velocity and the isoconcentration surface of 0.2 vol.% with mean flow velocity vectors (right) at 1200 s (A), 1800 s (B), 3600 s (C), 5400 s (D), 7200 s (E). Note that the white dashed outline (sediment concentration ≥0.2 vol.%) indicates its full extent. For visualisation purposes, the vertical topographic scale has been exaggerated tenfold to show the fold relief. Note the lines of longitudinal and transverse cross-sections shown in Fig. 4.

Table 3. Total volume [fraction] of bypassed sediment via linkage zone, fold crests and tips in Models 1 to 4.

Model code	Total volume [fraction] of bypassed sediment (m^3[vol.%])	Volume [fraction] of bypassed sediment via linkage zone (m^3[vol.%])	Volume [fraction] of bypassed sediment via upslope fold crest (m^3[vol.%])	Volume [fraction] of bypassed sediment via downslope fold crest (m^3[vol.%])	Volume [fraction] of bypassed sediment via upslope fold tip (m^3[vol.%])	Volume [fraction] of bypassed sediment via downslope fold tip (m^3[vol.%])
Model 1	127 127 246 [59]	19 209 030 [8.9]	7 953 256 [3.7]	23 977 106 [11.1]	16 883 061 [7.8]	59 104 794 [27.4]
Model 2	165 924 545 [77]	6 954 631 [3.2]	5 736 110 [2.7]	18 750 268 [8.7]	31 792 371 [14.7]	102 691 166 [47.5]
Model 3	159 924 863 [74]	28 817 232 [13.3]	19 240 533 [8.9]	51 801 664 [24.0]	12 376 823 [5.7]	47 688 611 [22.1]
Model 4	189 340 690 [88]	21 197 295 [9.8]	19 815 963 [9.2]	34 874 950 [16.1]	23 941 987 [11.1]	89 510 495 [41.4]

Note that total volumes of initial released suspended sediment are $2.16 \times 10^8\,m^3$ and overlapped fold segments are attributed to linkage zones to avoid triple-counting, with adjusted crest lengths.

Table 4. Total volume [fraction] of preferential deposited sediment (sand grain packing of ≥10 vol.%) in Models 1 to 4.

Model code	Total volume [volume fraction] of deposited sediment (m^3[vol.%])	Volume [volume fraction] of deposited sediment upslope of backlimbs (m^3[vol.%])	Volume [volume fraction] of deposited sediment along base of upslope fold backlimbs (m^3[vol.%])	Volume [volume fraction] of deposited sediment along base of downslope fold backlimbs (m^3[vol.%])	Volume [volume fraction] of deposited sediment at backlimbs (m^3[vol.%])
Model 1	59 800 359 [28]	3 476 421 [1.6]	10 313 760 [4.8]	33 619 428 [15.6]	1 351 068 [0.6]
Model 2	50 820 766 [24]	4 887 469 [2.3]	7 611 667 [3.5]	29 074 774 [13.5]	1 774 631 [0.8]
Model 3	47 857 680 [22]	5 143 980 [2.4]	15 570 949 [7.2]	16 578 615 [7.7]	2 147 471 [1.0]
Model 4	40 884 678 [19]	6 189 401 [2.9]	16 818 408 [7.8]	5 831 174 [2.7]	3 891 402 [1.8]

Note that total volumes of initial released suspended sediment are $2.16 \times 10^8\,m^3$ and accumulated sediment thicknesses <0.05 m are disregarded due to resolution limitation and systematical errors.

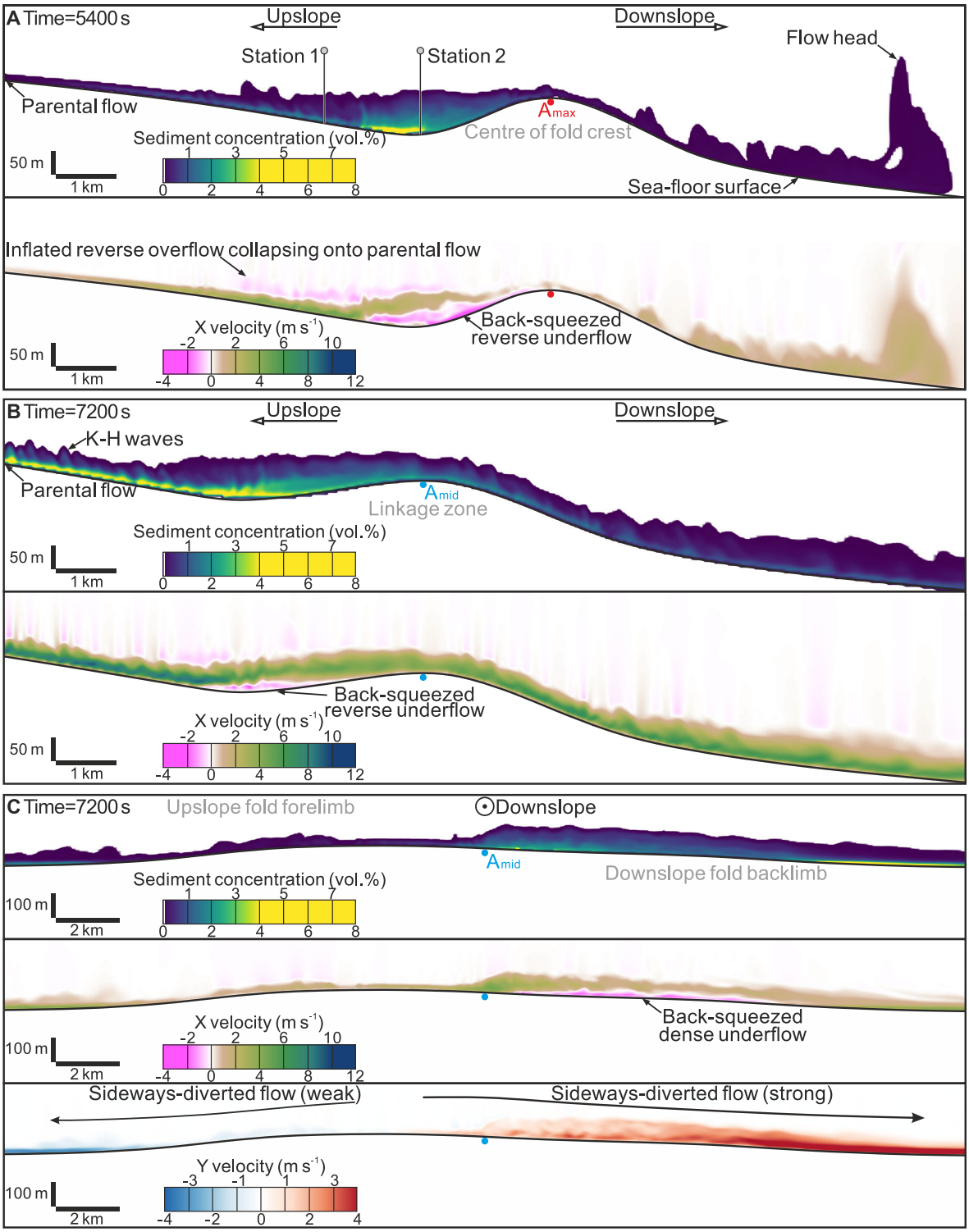

Fig. 4. Hydraulic longitudinal and transverse cross-sections of the flow approaching and overrunning segmented fold in Model 1 displayed in Fig. 3 (see the section lines therein). (A, B) Longitudinal cross-sections show the flow volumetric sediment concentration (top) and X velocity (bottom) of the flow approaching and overrunning the crests of upslope fold at 5400 s (A) and the centre of segmented fold at 7200 s (B). (C) Transverse cross-sections of the flow show the volumetric sediment concentration (top), X velocity (middle) and Y velocity (bottom) along the upslope fold forelimb and downslope fold backlimb at 7200 s. Note the reverse overflow and the reverse underflow in (A).

After 1200 s, the turbidity current approached the backlimb of the folds and decelerated over the next 600 s, with the flow thickening up to 100 m in the lower part of backlimb and gradually thinning towards the fold crest. While ascending the backlimb slope of ca 3° and diverging sideways along backlimb, the flow transitioned from supercritical to subcritical with the occurrence of hydraulic jumps upstream of the fold segments (Figs 3A to C and 6D to F). Also, as the flow encountered the backlimb of the fold, a reverse underflow developed as the locally decelerated and thickened parental flow was squeezed backwards (Fig. 4A and B). The reverse underflow, had a velocity of ca $-2\,m\,s^{-1}$ and sediment concentrations up to 6 vol.%, and transported suspended sediment up to 3-km upstream (Figs 4A and B, 5F and 6A and B). Upon reaching the base of the backlimb, the kinetic energy of the reverse underflow dissipated, causing the parental flow to rise and reflect as a dilute reverse overflow with a velocity of ca $-0.5\,m\,s^{-1}$ and sediment concentration up to 0.5 vol.% (Figs 4A and B and 5E). This reflected and inflated dilute suspension cloud extended up to 5 km further upstream than the underflow. The reverse overflow propagated back along the upper surface of the flow, slowing down the parental flow into a transient subcritical regime before collapsing (Figs 4A and B, 5 and 6D and E). Both the reverse overflow and the underflow weaken as the fold relief decreases along strike, and they interacted with the laterally spreading parental flow to form two bell-shaped reverse and subcritical flow systems (Figs 3C to E, 4A and B and 6D). The topographically induced transition from supercritical flow (i.e. $Fr > 1$) to subcritical flow (i.e. $Fr < 1$) occurred in a spatially confined and temporally steady region upslope of the segmented fold backlimb, termed here 'upstream hydraulic jumps' (Fig. 6D). These upstream hydraulic jumps typically occurred as relatively transient, low-frequency events, characterised by low-amplitude fluctuations (minimally ±0.2; e.g. Y-20 km in Fig. 6G and H) predominantly in the subcritical regime ($Fr < 1$) following such jumps.

The parental flow carried a diluted sediment suspension (ca 0.5 vol.%), with ca 3.7 vol.% of the total released sediment volume spilled over the upslope fold crest (Figs 3C to E and 4A). In contrast, 11.1 vol.% escaped across the downslope fold crest (Table 3). Once over fold crest, the subcritical flow accelerated again down the 4° forelimb slope and transformed into a supercritical flow with forward velocity increasing from $3\,m\,s^{-1}$ to $4.5\,m\,s^{-1}$ (Figs 4B and C and 6D to F). At the toe of fold forelimb, the flow slightly decelerated into subcritical with flow head thickness inflated from 50 m to nearly 250 m before accelerating into supercritical flow downstream and eventually reaching the limit of the simulation area at 5400 s (Figs 3D, 4B and C and 6D to F). The topographically induced transition from supercritical flow to subcritical flow at the base of the forelimb slope, are termed here as 'downstream hydraulic jumps' (Fig. 6D). In contrast to the upstream hydraulic jumps (Fig. 6D), a series of downstream hydraulic jumps occurred as continuous, high-frequency events (locally up to nearly 20 times; e.g. Y-10 km in Fig. 6G and H), characterised by the flow repeatedly transitioning between supercritical and subcritical regimes (*Fr* consistently fluctuating in the range of 0.5 to 1.5 with an amplitude of ca ±0.5; Fig. 6G and H).

In addition to reflection and overspill associated with the fold segments, the turbidity current interacted with the topography of the linkage zone. Longitudinally, 8.9 vol.% of the sediment was funnelled through the linkage zone within a relatively high velocity, $4\,m\,s^{-1}$, and concentrated, ca 2.5 vol.%, flow (Figs 3C to E, 4B and 13A and E). Transversely, the bulk of the flow exhibited asymmetric diversion along fold backlimbs, with substantial sediment transport redirected from the backlimb of the upslope fold to that of the downslope fold through the linkage zone unidirectionally (Figs 3C to E and 4C). Flow diversion by nearly 90° occurred at two key locations: (1) the centre of the linkage zone where the turbidity current diverted from longitudinal to transverse flow; and (2) the fold tips where the lateral turbidity current became convergent from transverse back to longitudinal flow (Fig. 3C to E). Consequently, 35.2 vol.% of the initial sediment volume bypassed around fold tips via twice diversions, ultimately spreading onto fold forelimbs. Marked flow asymmetry resulted in significantly greater sediment bypassed around the downslope fold tip (27.4 vol.%) than the upslope fold tip (7.8 vol.%) (Table 3).

Recognisable sediment deposition occurred extensively across the en-echelon segmented fold area, with ca 28 vol.% of the sediment released from the inlet gate deposited mainly in three zones (Fig. 5A, Table 4, Table S1): (i) a strike-parallel depozone upslope of each backlimb, up to 2.46 m in thickness and accounting

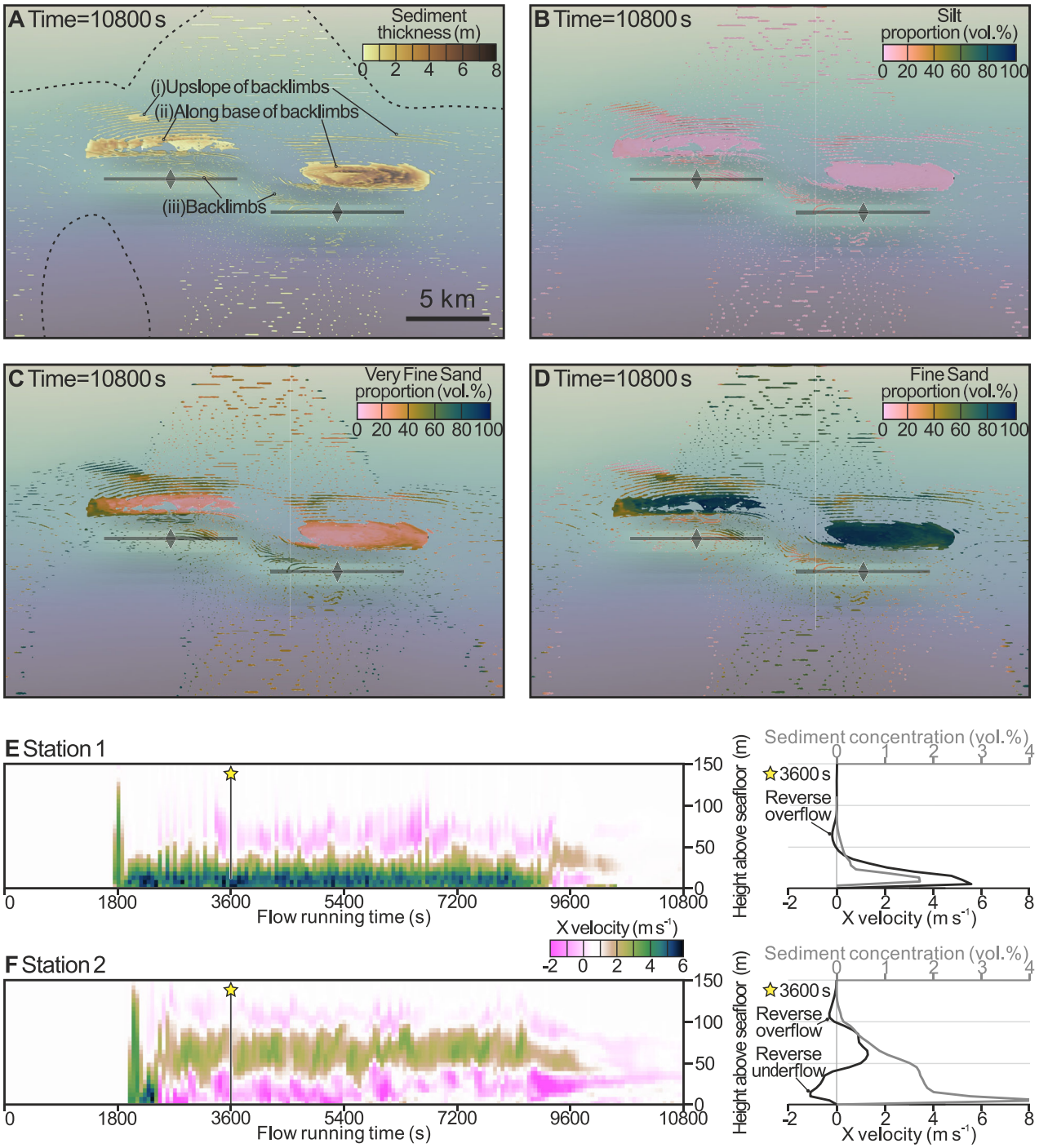

Fig. 5. Sediment preferential depozones and hydraulic parameters recorded at monitoring stations in Model 1. (A) Plan-view snapshot of sediment preferential depozones with total sand grain packing of ≥10 vol.% at 10 800 s. Note the area of accumulated sediment thickness <0.05 m is shown in white due to resolution limit and the black dashed outline indicates flow areal extent for mobile sand grain packing of ≥1 vol.%. For visualisation purposes, the vertical topographic scale has been exaggerated tenfold to show the fold relief. (B–D) Plan-view snapshots of sediment volume fraction for silt (B), very fine sand (C), and fine sand (D), showing areas where the total sand grain packing is ≥10 vol.% at 10 800 s. Note that the initial sediment was a mixture of 25 vol.% silt, 50 vol.% very fine sand, and 25 vol.% fine sand. (E, F) Time series and vertical profiles of the flow X velocity and volumetric sediment concentration at the two monitoring stations indicated in Figs 3D, 4A and 5B, with vertical profiles on the right illustrating the signatures of reverse overflow and underflow at 3600 s.

for 1.6 vol.%; (ii) a strike-parallel elliptical depozone along the base of each fold backlimb, up to 4.88 m in thickness (4.8 vol.%) on the upslope fold, and up to 9.12 m (15.6 vol.%) on the downslope fold; and (iii) a smaller transverse zone on each fold's backlimb slope, with a maximum

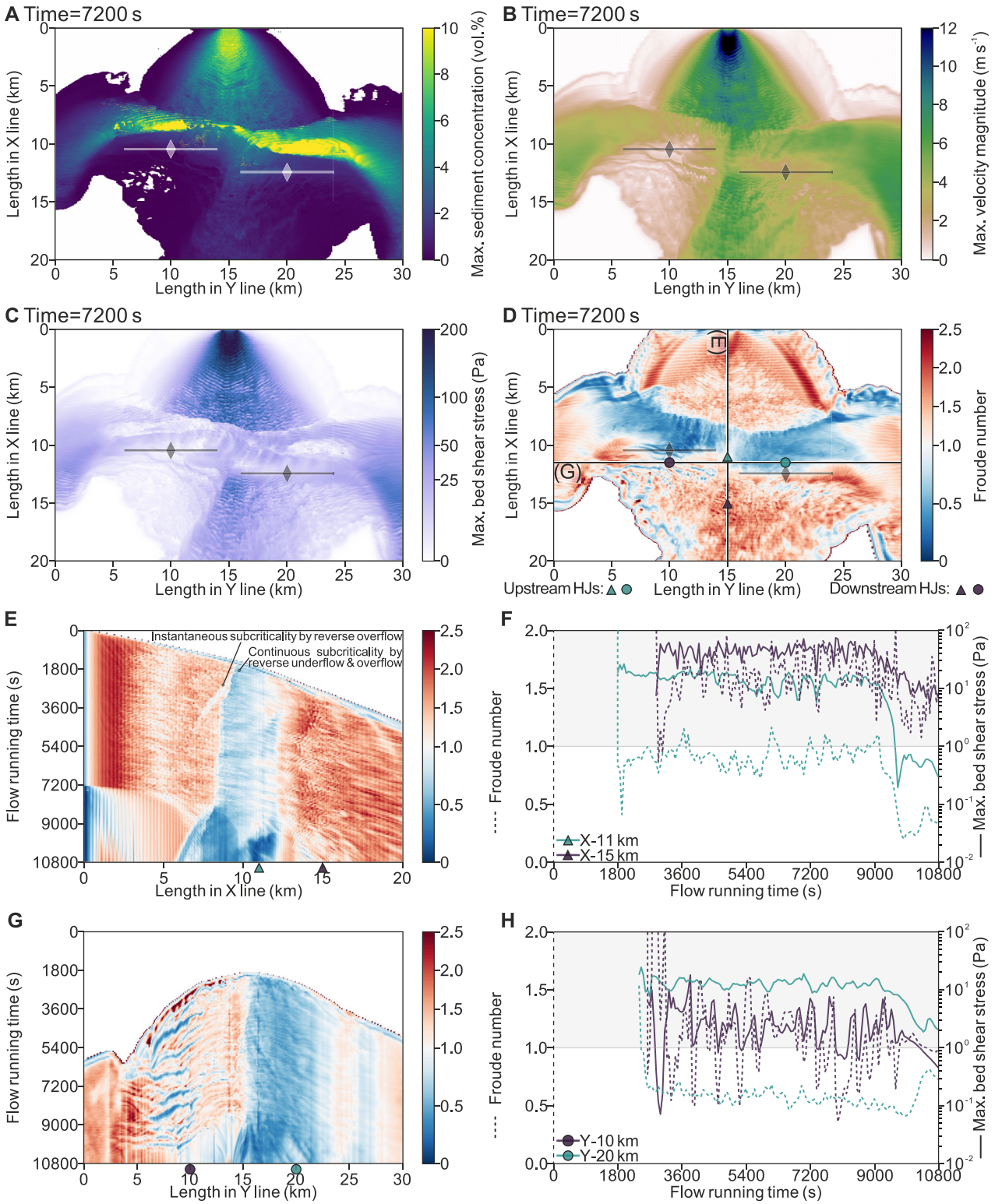

Fig. 6. Spatial heatmaps and time-series plots of hydraulic parameters in Model 1. (A–D) Spatial heatmaps of the flow Maximum sediment concentration (A), Maximum velocity magnitude (B), Maximum bed shear stress (C) and Froude number (*Fr*) (D) at 7200 s. See the Video S1 for more time-series details. Note the lines of longitudinal and transverse cross-sections shown in (E) and (G). (E) Time-series plots showing *Fr* fluctuations along the longitudinal section of turbidity currents (Y-15 km). (F) In-place fluctuations of the flow *Fr* (dashed line) and Maximum bed shear stress (solid line) at position of two triangles shown in (E), which correspond to the positions of the upstream and downstream hydraulic jumps. (G) Time-series plots showing *Fr* fluctuations along the transverse section of turbidity currents (X-11.5 km). (H) In-place fluctuations of the flow *Fr* (dashed line) and Maximum bed shear stress (solid line) at position of two dots shown in (G), which correspond to the positions of the upstream and downstream hydraulic jumps. Downstream HJs, downstream hydraulic jumps; Upstream HJs, upstream hydraulic jumps.

sediment thickness of 1.39 m (0.6 vol.%). The linkage zone exhibited limited sediment deposition, with only 0.11 vol.% of the total released sediment being deposited between the fold segments (Fig. 13E). Although the initial suspended sediment comprised 25 vol.% silt, 50 vol.% very fine sand and 25 vol.% fine sand, the grain-size distribution of deposited sediment varied spatially. Very fine sand dominated in depozones (i) and (iii), averaging ca 60 vol.%, whereas fine sand prevailed in depozones (ii), averaging ca 70 vol.% (Fig. 5B to D). In addition to sediment accumulation upstream of the fold, numerous dispersed and relatively thin deposits, predominantly fine sand, were also present on the downstream slope of the fold forelimb (Fig. 5A to D).

Model 2

Model 2 aims to assess the impact of en echelon segmented folds transitioning from separated along strike ($AlD = 2$ km) to overlapped ($AlD = -2$ km), whilst maintaining the same *AcD* (2 km) as in Model 1 (Fig. 2B, Table 2). Thus, Model 2 represents the late stage of oblique fold linkage with small *AcD* (<1/2 fold wavelength). Due to the overlap between fold segments, topographic relief in the linkage zone increases significantly, and the linkage ratio rises to 0.79 (Figs 2B, 7 and 8, Table 2).

In Model 2, the hydraulic behaviour of the turbidity current interacting with the two fold segments resembled a linked solitary fold with a deflected hinge (Fig. 7A to C). Similar to Model 1, subcritical flows upslope of the two merged folds exhibited a temporally steady distribution due to flow reflection associated with upstream hydraulic jumps. However, they differed from Model 1 in that no supercritical flow separation occurred (Fig. 8F). The linkage zone exhibited higher topographic relief, allowing fewer (3.2 vol.%), more diluted (ca 2 vol.%) and slower current (ca 3 m s^{-1}) stripping with downstream hydraulic jumps on the forelimb (Figs 7D and E, 8C to F and 13B and F). However, sediment bypass over and around the segmented fold topography was enhanced (reaching 77 vol.%; Table 3) due to the shorter effective blocking length caused by lateral fold-segment overlap. This was primarily driven by pronounced unidirectional flow diversion from the backlimb of the upslope fold to that of the downslope fold across the linkage zone (Figs 7 and 8B). Consequently, sediment bypass around the downslope fold tip (47.5 vol.%) significantly exceeded that around the upslope fold tip (14.7 vol.%). Furthermore, sediment carried by the dilute turbidity current spilling over the downslope fold crest was more than triple that over the upslope fold crest (8.7 and 2.7 vol.%, respectively) (Fig. 7A to C, Table 3).

Fold-segment overlap not only enhanced overall sediment bypass but also reduced deposition to 24 vol.% (Fig. 8A, Table 4). The depozone configuration in Model 2 resembled that in Model 1, where marked flow asymmetry resulted in a more extensive depozone distribution along the base of downslope fold backlimb. This zone received a significantly higher proportion of deposited sediment (13.5 vol.%) compared to the upslope fold (3.5 vol.%) (Fig. 8A, Table 4). As in Model 1, the linkage zone had limited deposition, with only 0.16 vol.% of total released sediment deposited between the two overlapping fold segments. This minimal deposition occurred through sediment transport via ascending dilute waning flows (Fig. 13F).

Model 3

Model 3 aims to evaluate the influence of increased across-strike spacing ($AcD = 4$ km)

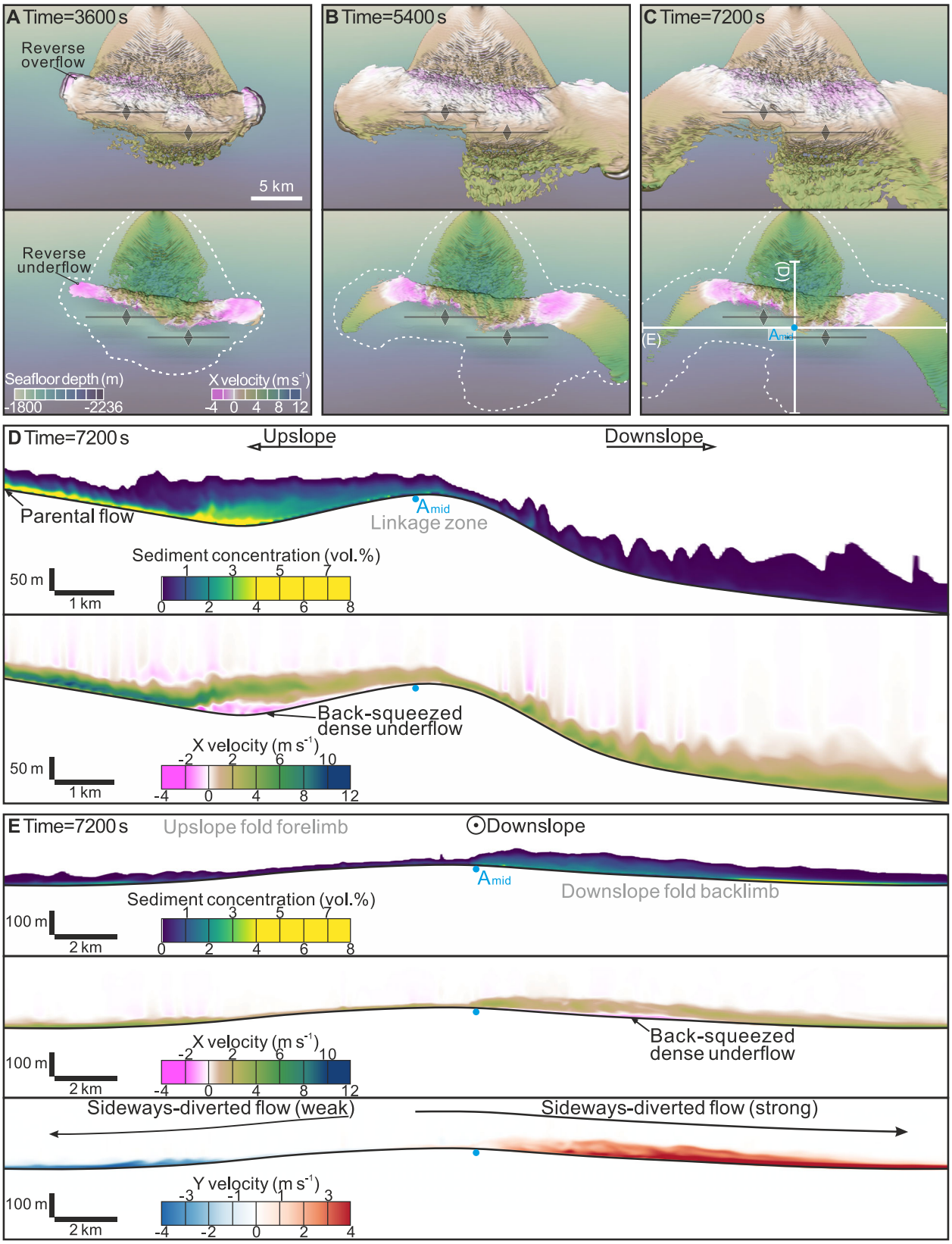

Fig. 7. Hydraulic behaviours of turbidity currents in response to segmented fold in Model 2 (Table 2). (A–C) Plan-view snapshots of the flow sediment isoconcentration surface of 0.2 vol.% (top) and 0.8 vol.% (bottom) with X velocity as colour scale at 3600 s (A), 5400 s (B) and 7200 s (C). For visualisation purposes, the vertical topographic scale has been exaggerated tenfold to show the fold relief. Note the lines of longitudinal and transverse cross-sections shown in (D) and (E). (D) Hydraulic longitudinal cross-sections of the flow approaching and overrunning the centre of segmented fold (A_{mid}) show the flow volumetric sediment concentration (top) and X velocity (bottom) at 7200 s. (E) Hydraulic transverse cross-sections of the flow show the volumetric sediment concentration (top), X velocity (middle) and Y velocity (bottom) along the upslope fold forelimb and downslope fold backlimb at 7200 s.

between en-echelon segmented folds while maintaining the same along-strike spacing as in Model 1 ($AlD = 2$ km). This represents the early stage of oblique fold linkage with large AcD (≥1/2 fold wavelength) (Fig. 2C, Table 2). The linkage zone features a longitudinal depression broadly developed between fold culminations and exhibits low relief with a linkage ratio of 0.27 (Figs 2C, 9 and 10, Table 2).

The increase in AcD allowed turbidity current entering the linkage zone with sufficient distance to re-accelerate (Fig. 9A to C), achieving a time-averaged maximum velocity of ca 6.5 m s^{-1} and maximum sediment concentration of ca 2 vol.% (Fig. 13C). Consequently, supercritical flow facilitated direct bypass of a significantly greater sediment fraction (13.3 vol.%) through the linkage zone, without generating reflected reverse underflow or overflow (Figs 9D and E, 10F and 13G). Flow reflection decoupling along the backlimbs of the en-echelon segmented fold promoted spillover of dilute turbidity current over fold crests, accounting for ca 33 vol.% of the total sediment load (Fig. 9, Table 3). Notably, spillover from the downslope fold crest reached 24 vol.%, whereas the upslope fold crest contributed only 8.9 vol.%. This substantial crestal spillover and bypass through the linkage zone reduced sediment bypass around fold tips correspondingly, reducing the downslope fold tip bypass to 22.1 vol.% (Fig. 9C, Table 3).

These changes collectively reduced total sediment deposition to 22 vol.% (Fig. 10A, Table 4). Although diversion asymmetry persisted (Fig. 10B), pronounced spillover from the downslope fold crest reduced deposition along the base of its backlimb, resulting in nearly equivalent sediment volumes deposited along the bases of upslope (7.2 vol.%) and downslope (7.7 vol.%) fold backlimbs (Fig. 10A, Table 4). Despite enhanced longitudinal flow routing through the linkage zone to the fold forelimbs, this region exhibited minimal sediment deposition, retaining only 0.02 vol.% of the total released sediment.

Model 4

Model 4 aims to assess the impact of en echelon segmented folds transitioning from separated ($AlD = 2$ km) to overlapped ($AlD = -2$ km) along strike while keeping the same across-strike distance ($AcD = 4$ km) as Model 3 (Fig. 2D, Table 2). The resultant fold topography resembles the late stage of oblique fold linkage of folds with wide spacing (≥1/2 fold wavelength). Within the overlapped linkage zone, a prominent basinward-plunging longitudinal depression develops, oriented subparallel to the two fold segments and displaying a low linkage ratio of 0.14 (Figs 2D, 11 and 12, Table 2).

In addition to flow diversion from the upslope fold backlimb to the downslope fold backlimb that is present in the previous three models, Model 4 exhibited a portion of the flow that is redirected from the backlimb of the downslope fold into the overlapped linkage zone (Figs 11 and 12). This formed a localised sideways-diverted reverse underflow that emerged around 5400 s (Figs 11E, 12B and 13D). Consequently, although the along-strike overlap prevented direct turbidity current bypass through the linkage zone, the sufficiently large across-strike separation distance and bidirectional flow diversion sustained the linkage zone as a significant flow pathway (Figs 11A to D and 12C to F). A substantial sediment fraction (9.8 vol.%) was diverted directly through the linkage zone with enhanced sediment concentration (increasing from ca 1.5 to 3 vol.%), but reduced velocity (decelerating from ca 6 to 4 m s^{-1}) (Figs 11 and 13D and H, Table 3). Furthermore, spillover from the downslope fold crest decreased to 16.1 vol.% compared with Model 3, still exceeding that of

upslope fold with 9.2 vol.% (Fig. 11A to C, Table 3). The large fold segment overlap resulted in a relatively short diversion path around the downslope fold tip and significantly greater sediment bypass (41.4 vol.%) compared to the upslope fold tip (11.1 vol.%) (Table 3).

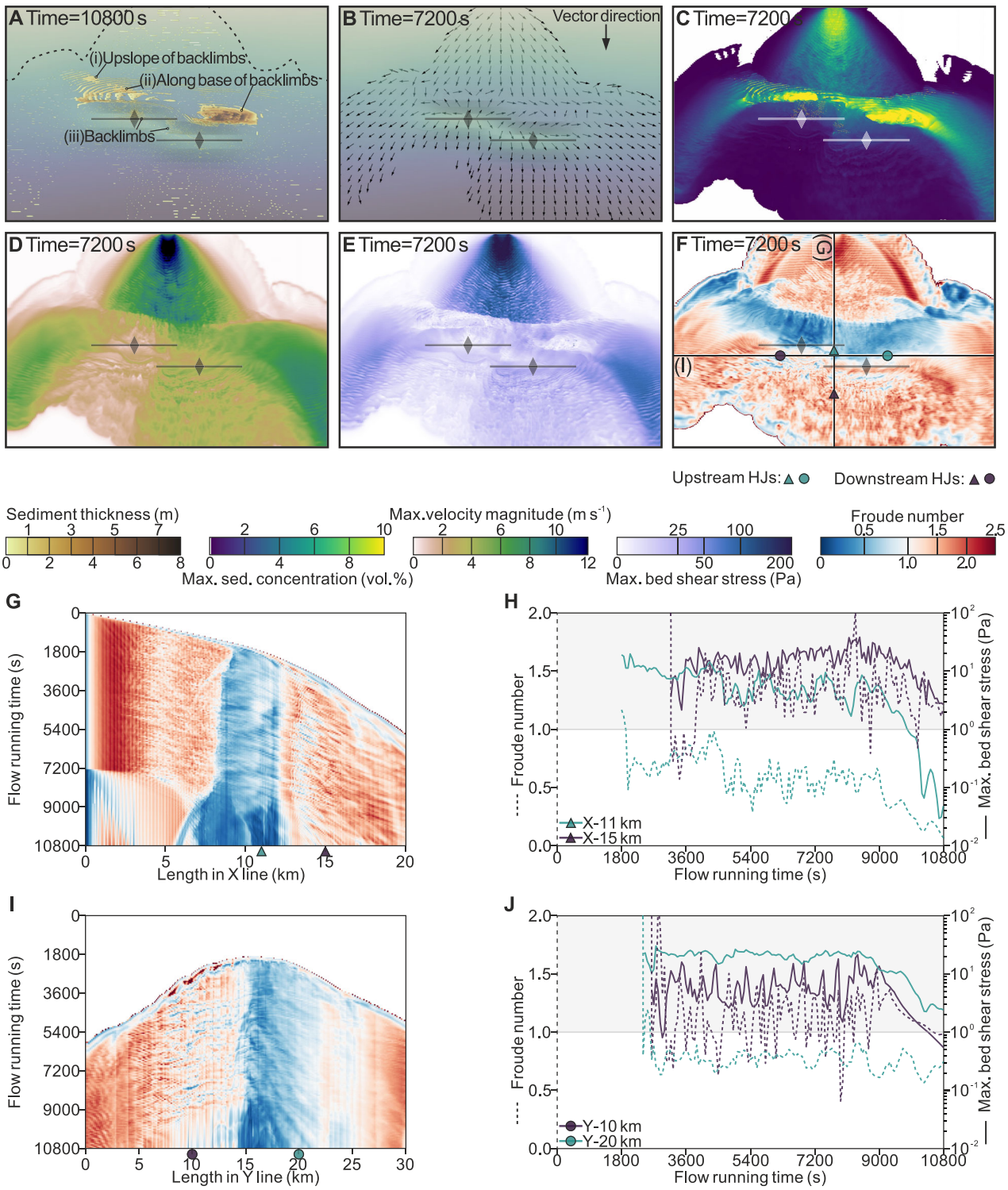

Fig. 8. Flow behaviours and sedimentary characteristics in Model 2. (A) Plan-view snapshot of sediment preferential depozones with total sand grain packing of ≥10 vol.% at 10 800 s. Note the area of accumulated sediment thickness <0.05 m is shown in white due to resolution limit and the black dashed outline indicates flow areal extent for mobile sand grain packing of ≥1 vol.%. (B) Plan-view snapshots of the flow sediment isoconcentration surface of 0.2 vol.% with mean flow velocity vectors at 7200 s. (C–F) Spatial heatmaps of the flow Maximum sediment concentration (C), Maximum velocity magnitude (D), Maximum bed shear stress (E) and Froude number (*Fr*) (F) at 7200 s. See the Video S2 for more time-series details. Note the lines of longitudinal and transverse cross-sections shown in (G) and (I). (G) Time-series plots showing *Fr* fluctuations along the longitudinal section of turbidity currents (Y-15 km). (H) In-place fluctuations of the flow *Fr* (dashed line) and Maximum bed shear stress (solid line) at position of two triangles shown in (G), which correspond to the positions of the upstream and downstream hydraulic jumps. (I) Time-series plots showing *Fr* fluctuations along the transverse section of turbidity currents (X-11.5 km). (J) In-place fluctuations of the flow *Fr* (dashed line) and Maximum bed shear stress (solid line) at position of two dots shown in (I), which correspond to the positions of the upstream and downstream hydraulic jumps. Downstream HJs, downstream hydraulic jumps; Upstream HJs, upstream hydraulic jumps.

The combined effect of increased across-strike separation distance and greater segment overlap reduced total sediment deposition to 19 vol.%, the minimum value among the four models (Fig. 12A, Table 4). Critically, compared to Model 3, the deposited sediment volume along the base of downslope fold backlimb decreased significantly to 2.7 vol.%, which is less than half the 7.8 vol.% deposited along upslope fold backlimb (Fig. 12A, Table 4). Meanwhile, the linkage zone retained minimal sediment deposition (0.07 vol.%) (Fig. 13H, Table 4).

DISCUSSION

This study establishes the first systematic framework for analysing the hydraulic response of large, natural-scale unconfined turbidity currents to en-echelon segmented folds. Four distinct fold configurations (Models 1 to 4) represent different across-strike separation and along-strike overlap that are typical of natural segmented fold arrays. We demonstrate how linkage zone architecture fundamentally controls flow partitioning and basinward sediment bypass. Despite significant hydraulic and depositional variations within linkage zones, fold topography is identified as the primary control on turbidity current hydrodynamics, governed by distinct types of topographically induced hydraulic jumps. In the discussion, we focus on how fold topography controls turbidity current hydrodynamics, the impact of en-echelon segmented folds on flow behaviour and sediment deposition, and comment on some of the limitations of this study.

Fold topography as a primary control on turbidity current hydrodynamics

Fold-related topography exerts a first-order control on the hydraulic response of turbidity currents, creating distinct flow patterns upstream and downstream of the segmented folds. In all our models, the flow decelerates and thickens twice: firstly on the fold backlimb, and secondly at the base of the forelimb slope. This general flow pattern in response to topographic obstacles is similar to that reported by previous laboratory experiments (Rottman & Simpson, 1989; Edwards *et al.*, 1994; Lamb *et al.*, 2006), numerical simulations (Howlett *et al.*, 2019) and field observations of outcrops in Apennine and Alpine foreland basins (Tinterri *et al.*, 2016, 2022; Tinterri & Piazza, 2019). The present study demonstrates that the occurrence of two distinct types of topographically induced transition from supercritical flow to subcritical flow are directly related to the aforementioned two deceleration and thickening processes, namely upstream and downstream hydraulic jumps. These transitions exhibit significant differences in their occurrence and fluctuations of *Fr* (Fig. 6H). Such differences are attributed to variations in turbidity current energy fluctuations, which generate interfacial Kelvin–Helmholtz (K–H) waves of varying amplitudes.

When the turbidity current encounters fold topography it is partially reflected, and the forward-travelling parental flow becomes sandwiched between a lower back-squeezed dense reverse underflow, and an upper inflated dilute reverse overflow (Figs 3 and 4A and B). Both the reverse overflow and underflow decrease the

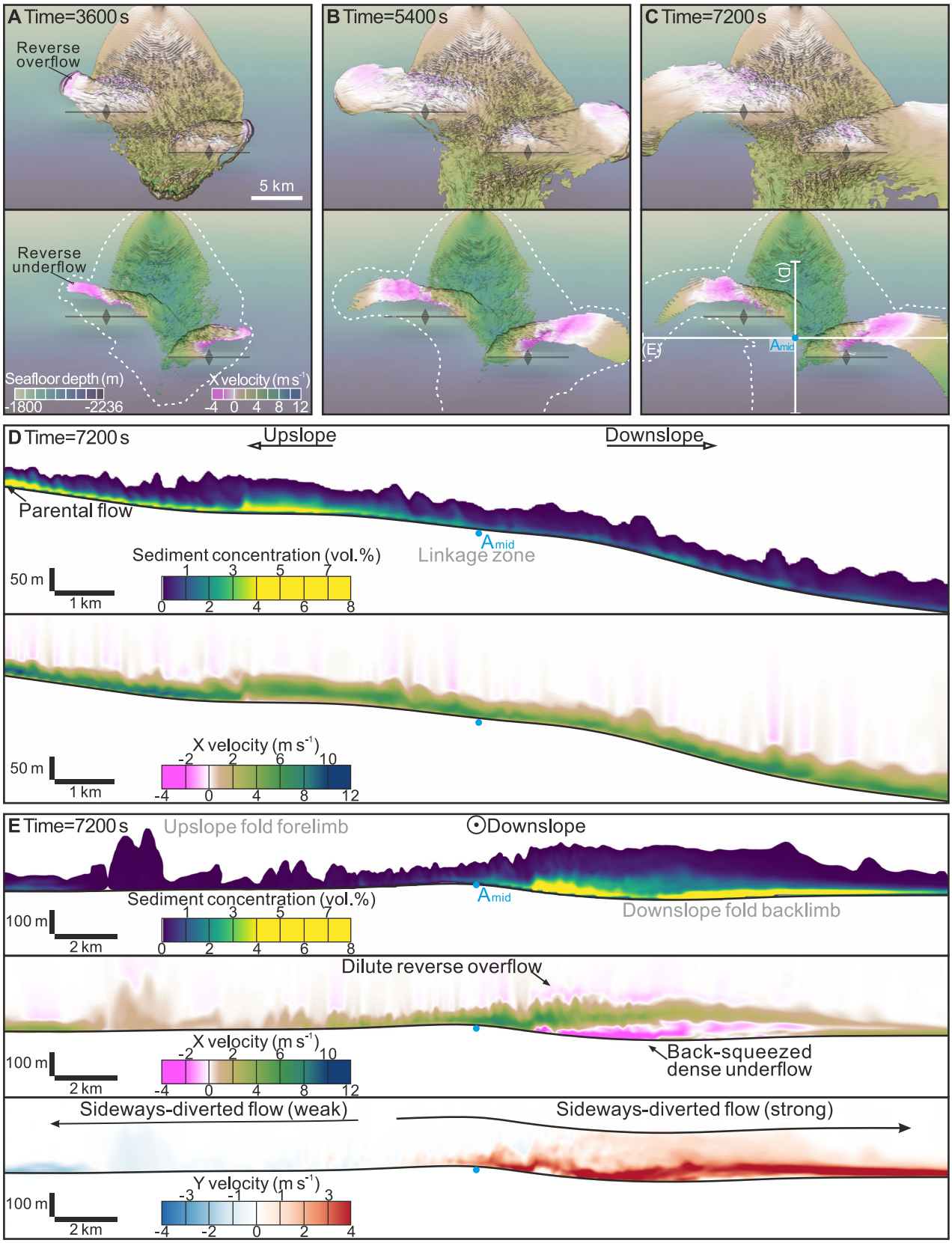

Fig. 9. Hydraulic behaviours of turbidity currents in response to segmented fold in Model 3 (Table 2). (A–C) Plan-view snapshots of the flow sediment isoconcentration surface of 0.2 vol.% (top) and 0.8 vol.% (bottom) with X velocity as colour scale at 3600 s (A), 5400 s (B) and 7200 s (C). For visualisation purposes, the vertical topographic scale has been exaggerated tenfold to show the fold relief. Note the lines of longitudinal and transverse cross-sections shown in (D) and (E). (D) Hydraulic longitudinal cross-sections of the flow approaching and overrunning the centre of segmented fold (A_{mid}) show the flow volumetric sediment concentration (top) and X velocity (bottom) at 7200 s. (E) Hydraulic transverse cross-sections of the flow show the volumetric sediment concentration (top), X velocity (middle) and Y velocity (bottom) along the upslope fold forelimb and downslope fold backlimb at 7200 s.

waning rate of parental flow through sediment suspension feedback and extend their runout via the recharging effect (Fig. 5E and F) (see Howlett *et al.*, 2019; Tinterri *et al.*, 2022). The upstream inflation and deceleration of this reverse flow exhibit strong longitudinal and transversal variations, forming two connected or isolated bell-shaped subcritical flow systems with upstream hydraulic jumps (Figs 6D and 10F). Following the low-frequency upstream hydraulic jumps with criticality transition, the flow exhibits low-amplitude fluctuations of *Fr* while remaining subcritical during the course ($Fr < 1$) (Figs 6E to H, 8G to J, 10G to J and 12G to J). Moreover, the kinetic energy of turbidity currents dissipates as the parental flow is raised by reverse underflow and reflected backwards as reverse overflow, forming a linear standing-wave billows (Alexander & Morris, 1994) along the base of fold backlimb (Fig. 3D). These billows represent a topographically induced smoothing of the flow boundary (Pantin & Leeder, 1987), accompanied by prominent suppression of K–H waves (Figs 4A and B and 5).

On the gentler forelimb slope, the overspilled supercritical turbidity current rapidly decelerates and thickens, and undergoes a transition from proximal bypass to distal deposition (Figs 4A and B and 6B). During the process, high-frequency downstream hydraulic jumps occur, marked by high-amplitude fluctuations in *Fr* alternating between subcritical and supercritical regimes (Fig. 14). These frequent jumps resemble supercritical-to-subcritical transitions in cyclic steps between the lee and stoss sides (Slootman & Cartigny, 2020; Maselli *et al.*, 2021; Englert *et al.*, 2023). Unlike upstream hydraulic jumps, downstream hydraulic jumps dissipate turbidity current kinetic energy through enhanced turbulence, generating large-scale K–H waves (Komar, 1971). Consequently, such hydraulic jump causes instantaneous changes in bed shear stress along the toe of fold forelimb (Figs 6H and 8J), increasing local erosion potential and generating features such as seafloor scours (Sumner *et al.*, 2013). Along the downstream of the forelimb, these jumps significantly reduce bed shear stress (Figs 6C and 8E), promoting substantial bedload deposition from turbidity currents (Garcia & Parker, 1989; Garcia, 1993). This mechanism explains enigmatic seafloor features downstream of slope breaks, ranging from proximal erosional scour fields to distal depositional sediment wave fields, commonly observed in channel-lobe transition zones (CLTZs) (Wynn *et al.*, 2002; Hodgson *et al.*, 2022). Specifically, once depositional topography becomes sufficiently elevated to form hydraulic-jump unit bars that obstruct flow, the downstream hydraulic jumps may transform into upstream hydraulic jumps (MacDonald *et al.*, 2009; Pohl *et al.*, 2019; Smith *et al.*, 2020). Our study suggests such transitions bear fundamental changes in hydraulic characteristics.

Impact of en-echelon segmented folds on flow behaviour

Previous research has highlighted the importance of segmented fold topography on turbidity current dynamics, particularly the role of segment boundary relief (Morley, 2009; Howlett *et al.*, 2021; Pizzi *et al.*, 2023). Our findings suggest that segment boundaries can act either as a crucial zone for flow transfer and redirection or as an obstacle blocking flow. The exact role that a segment boundary may play depends on the configuration of the fold boundary and the evolutionary stage of the segmented folds.

At an early stage of linkage of en-echelon segmented folds, due to a low linkage ratio (e.g. Model 1 and Model 3), segment boundaries exhibit relatively low topographic relief. Turbidity currents either flow directly through these

low topography segment boundaries, or are diverted obliquely along fold backlimbs through the boundaries (Figs 3 and 9). Flow acceleration and intensified erosion occur at segment boundaries due to lateral confinement by growing fold flanks (Figs 6A to D, 10C to F and 13A and C). This flow constriction mechanism (or 'flow convergence', Soutter *et al.*, 2021)

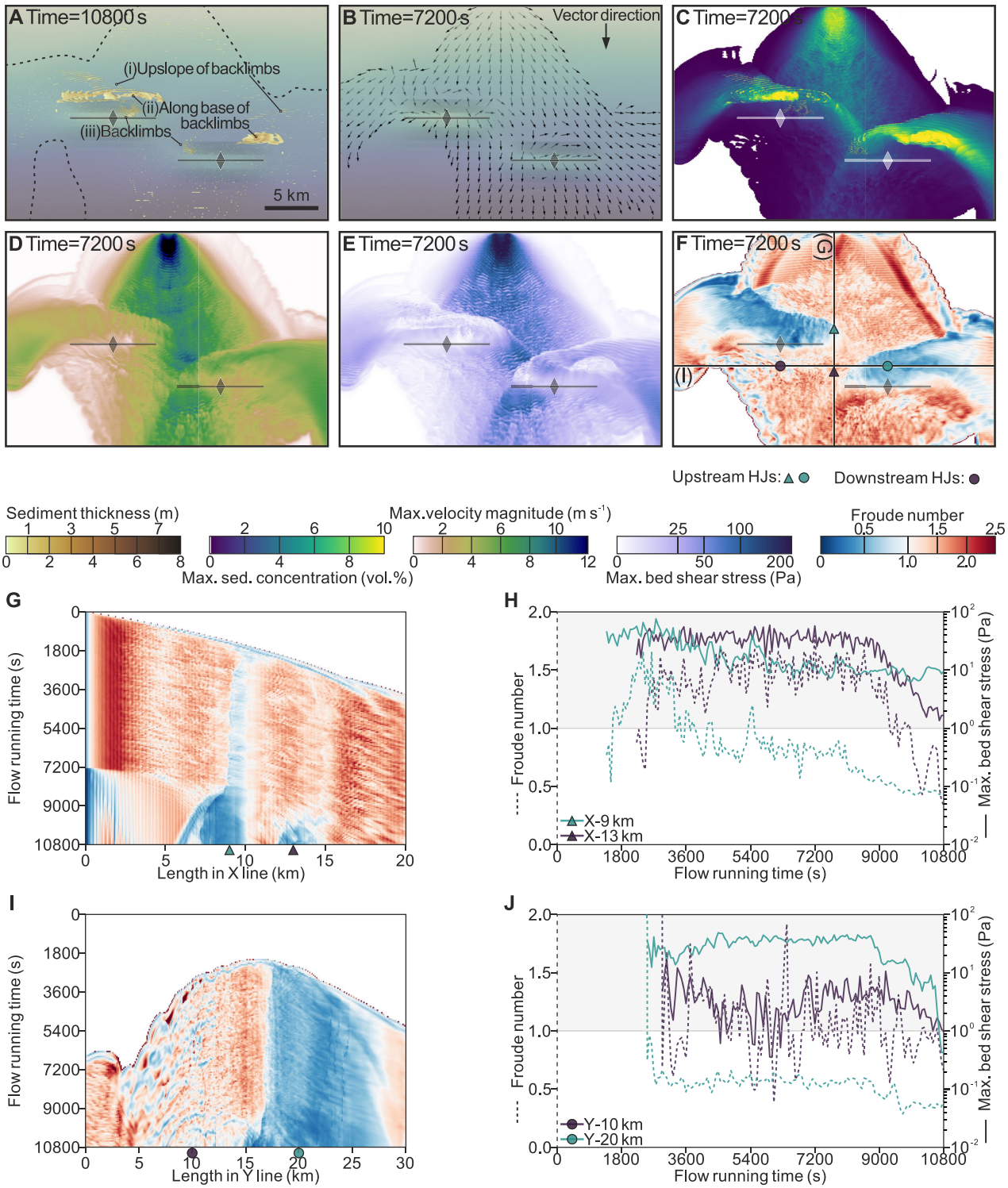

Fig. 10. Flow behaviours and sedimentary characteristics in Model 3. (A) Plan-view snapshot of sediment preferential depozones with total sand grain packing of ≥10 vol.% at 10 800 s. Note the area of accumulated sediment thickness <0.05 m is shown in white due to resolution limit and the black dashed outline indicates flow areal extent for mobile sand grain packing of ≥1 vol.%. (B) Plan-view snapshots of the flow sediment isoconcentration surface of 0.2 vol.% with mean flow velocity vectors at 7200 s. (C–F) Spatial heatmaps of the flow Maximum sediment concentration (C), Maximum velocity magnitude (D), Maximum bed shear stress (E) and Froude number (*Fr*) (F) at 7200 s. See the Video S3 for more time-series details. Note the lines of longitudinal and transverse cross-sections shown in (G) and (I). (G) Time-series plots showing *Fr* fluctuations along the longitudinal section of turbidity currents (Y-15 km). (H) In-place fluctuations of the flow *Fr* (dashed line) and Maximum bed shear stress (solid line) at position of two triangles shown in (G), which correspond to the positions of the upstream hydraulic jumps. (I) Time-series plots showing *Fr* fluctuations along the transverse section of turbidity currents (X-12.5 km). (J) In-place fluctuations of the flow *Fr* (dashed line) and Maximum bed shear stress (solid line) at position of two dots shown in (I), which correspond to the positions of the upstream and downstream hydraulic jumps. Downstream HJs, downstream hydraulic jumps; Upstream HJs, upstream hydraulic jumps.

corresponds to observations from seismic reflection data of vertically stacked channels showing increased incision depth and reduced sinuosity in segment boundaries (Gee *et al.*, 2001; Jolly *et al.*, 2017; Howlett *et al.*, 2021; Mitchell *et al.*, 2021a,b, 2022; Pizzi *et al.*, 2023).

At a later stage of the linkage process, the impact of segment boundaries on turbidity currents is contingent upon whether the across-strike distance (*AcD*) exceeds half of the fold wavelength (Grasemann & Schmalholz, 2012). In the case of small *AcD* (<1/2 fold wavelength), mature folds develop pronounced longitudinal relief and subtle transverse depressions with a higher linkage ratio (e.g. Model 2). As turbidity currents flow into the depression between two culminations, the main flow experiences deceleration, reflection and upstream hydraulic jumps, resulting in locally decreased bed shear stress (Figs 7 and 8B to F). This is manifested as the channel system in nature being partially healed over the initial incision by continuous backfilling deposits upstream of the segment boundary, or being diverted sideways along fold backlimbs to surround fold tips with aggradational levees (Clark & Cartwright, 2009, 2011, 2012; Howlett *et al.*, 2021; McArthur *et al.*, 2022). Furthermore, the segment boundary permits spillover of volumetrically small, unconfined current funnelled through the topographic constriction, which then experiences downstream hydraulic jumps with frequent and abrupt fluctuations in bed shear stresses (Figs 8G and H and 13B). Such downstream hydraulic jumps, which may induce scouring and initiate deep-water channel erosion, have also been documented as channel-margin slumping and degradation complexes near the forelimb in the Niger Delta slope and NW margin of Borneo (Heiniö & Davies, 2007; Morley, 2009).

In the case of large *AcD* (≥1/2 fold wavelength), the linkage ratio decreases with fold lateral growth (from Model 3 to Model 4), still maintaining a low-relief conduit along the segment boundary even after folds overlap along strike. The low-relief segment boundary remains an efficient pathway for sediment transport, facilitating downslope movement of near-bed, high-concentration sediments from laterally diverted reverse underflows (Figs 11, 12B and 13D). Such significant flow pathways between folds were also recognised around the DWFTBs in the Niger Delta, where meandering channels develop along strike from the upslope fold tip to that of downslope fold through the overlapping region (Clark & Cartwright, 2012; Don *et al.*, 2020).

Influence of en-echelon segmented folds on sediment dispersal pattern

Previous numerical simulations indicate sediment dispersal exhibits a patchy spatial distribution within fold-relief topography, primarily controlled by turbidity currents' hydraulics (Howlett *et al.*, 2019). In addition to the deposition outside the inlet gate, which is an artefact of the flow self-regulation before reaching a quasi-steady supercritical regime (Ge *et al.*, 2017), our study reveals the pattern of deposition by unconfined turbidity current

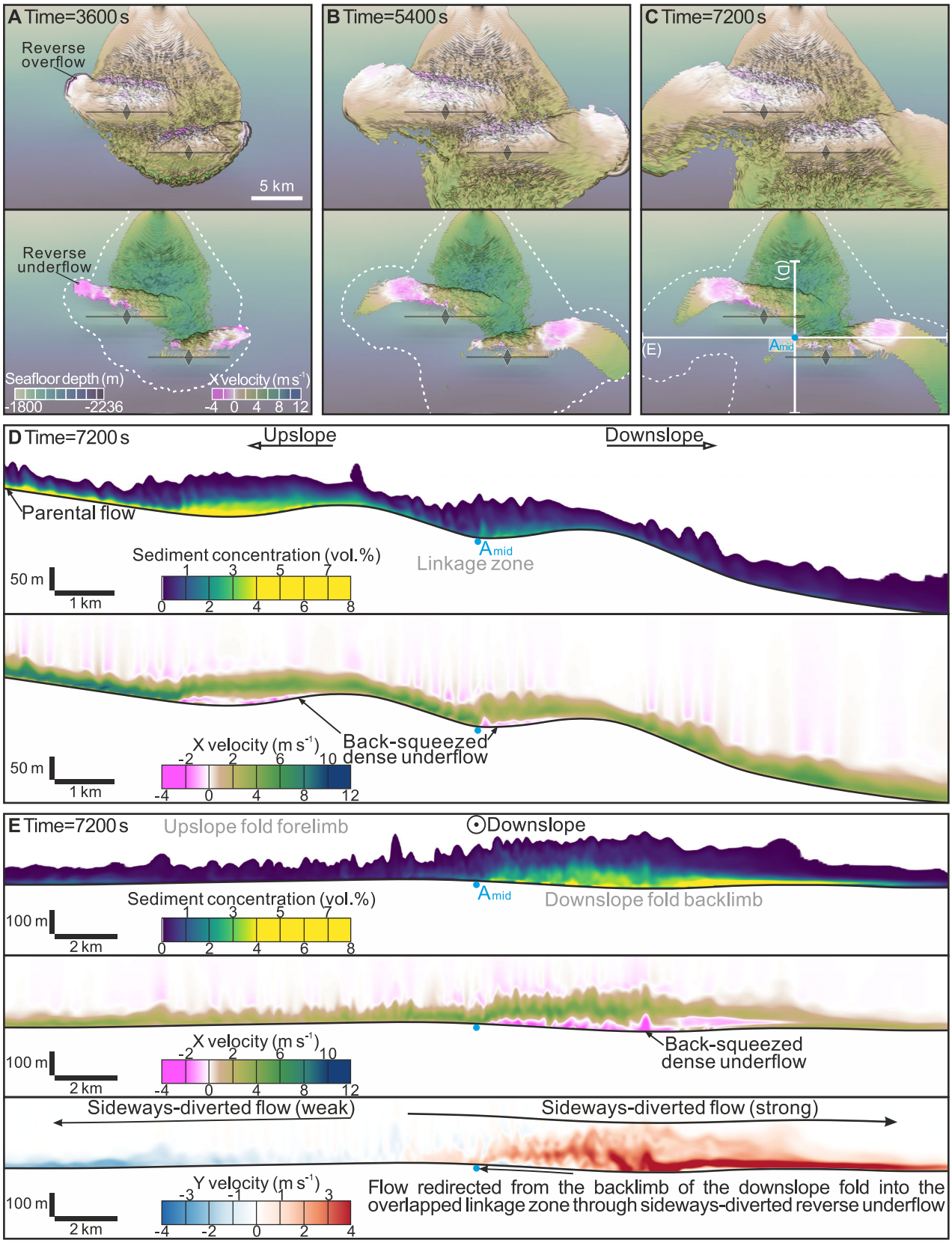

Fig. 11. Hydraulic behaviours of turbidity currents in response to segmented fold in Model 4 (Table 2). (A–C) Plan-view snapshots of the flow sediment isoconcentration surface of 0.2 vol.% (top) and 0.8 vol.% (bottom) with X velocity as colour scale at 3600 s (A), 5400 s (B) and 7200 s (C). For visualisation purposes, the vertical topographic scale has been exaggerated tenfold to show the fold relief. Note the lines of longitudinal and transverse cross-sections shown in (D) and (E). (D) Hydraulic longitudinal cross-sections of the flow approaching and overrunning the centre of segmented fold (A_{mid}) show the flow volumetric sediment concentration (top) and X velocity (bottom) at 7200 s. (E) Hydraulic transverse cross-sections of the flow show the volumetric sediment concentration (top), X velocity (middle) and Y velocity (bottom) along the upslope fold forelimb and downslope fold backlimb at 7200 s.

around en-echelon segmented fold is dominated by topographically induced upstream and downstream hydraulic jumps.

Our modelling results show that sedimentation associated with upstream hydraulic jumps predominantly occurs in three distinct depozones, described and discussed below from proximal to distal relative to the flow inlet. Firstly, strike-parallel depozones upslope of backlimb (i), that are located progressively further upstream of the backlimb from the axis of flow to edge (Figs 5A, 8A, 10A and 12A, Table 4, Table S1). This depozone results from upstream migration of reverse overflow bores, evidenced by flow thickening boundaries raised by reverse underflow (Fig. 3). Secondly, strike-parallel elliptical depozones along the base of the backlimbs of both upslope and downslope folds (ii), with thickness up to ca 9 m (Figs 5A, 8A, 10A and 12A, Table 4, Table S1). This depozone is situated within the parental flow thickening area, induced by reverse underflow. Sediment accumulation here stems from backward squeezing of dense near-bed flow, with lateral influence from where the flow is diverted (Figs 3 and 4). Thirdly, localised transverse zones on fold backlimbs (iii) (Figs 5A, 8A, 10A and 12A, Table 4, Table S1) formed by ascending dilute waning flow at segment boundaries with reduced sand deposition. Coarser sediments are predominantly deposited directly at the bases of fold backlimbs (ii) due to basal dense reverse underflow (Figs 4 and 5). Finer sediments, however, are deposited either upslope of the fold backlimbs (i) or on fold backlimbs (iii) through upper dilute reverse overflow or flow superelevation (Muck & Underwood, 1990; Soutter *et al.*, 2021). In addition to concentrated sediment accumulation upstream of the fold, significant but scattered sediment deposition occurs downstream of fold forelimbs. These deposits result from flow stripping of overspilled turbidity currents, where deposition progressively thickens downslope due to downstream hydraulic jumps and amplification of Kelvin–Helmholtz waves (Figs 4B and 5A to D). These observations align with the experimental findings of Garcia & Parker (1989), in which the sediment thickness increases downstream has been documented along with hydraulic jumps.

The growth and linkage of en-echelon segmented folds control the topographic evolution and associated depocentre migration (Fig. 14). In general, across-strike distance (*AcD*) is established during fold initial nucleation, whereas along-strike distance (*AlD*) gradually decreases during fold growth by lateral propagation, and eventually stabilises once folds become hard linked (Ramsey *et al.*, 2008; Fernandez & Kaus, 2014a; Zhang *et al.*, 2021; Gao *et al.*, 2023). Sediment deposition decreases during oblique linkage of two en-echelon fold segments, with depocentre migrating from the base of downslope fold backlimb to that of upslope fold as *AcD* increases (Figs 5A, 8A, 10A and 12A, Table 4). When the *AcD* is small (<1/2 fold wavelength; e.g. Model 1 & Model 2, Figs 2A and B and 14A and B), asymmetrical flow diversion promotes greater sediment accumulation at the base of downslope fold backlimb. However, late-stage development of the overlapped linkage zones diminishes sediment accumulation at bases of both fold backlimbs (Figs 5A and 8A). When the *AcD* is large (≥1/2 fold wavelength; e.g. Model 3 & Model 4, Figs 2C and D and 14C and D), increased separation between fold segments creates a low relief linkage zone that serves as an effective conduit for sediment-laden flow, resulting in reduced sediment deposition (Figs. 9 to 12, Table 4). As folds grow and they overlap, confined flow reflection and bidirectional diversion transport sediment away from the downslope fold backlimb (Fig. 11E), resulting in less sediment accumulation compared to the upslope fold (Fig. 12A; Table 4).

Our models reveal the three-dimensional sedimentary dynamics within DWFTBs (Fig. 14), combining elements from classical 2D

sedimentary models: the 'fill-and-spill' model (e.g. Beaubouef & Friedmann, 2000; Sinclair & Tomasso, 2002) and the strike-confined 'tortuous corridors' model (Smith, 2004). Approximately 20 to 30 vol.% of the total initially released sediment is captured by segmented fold backlimbs (Table 4), creating a dynamic topographic configuration. Sediment retained within the turbidity current is transported downslope by spillover across fold crests and linkage zones or diversion around fold tips, thereby bypassing proximal intra-slope basins as conceptualised by

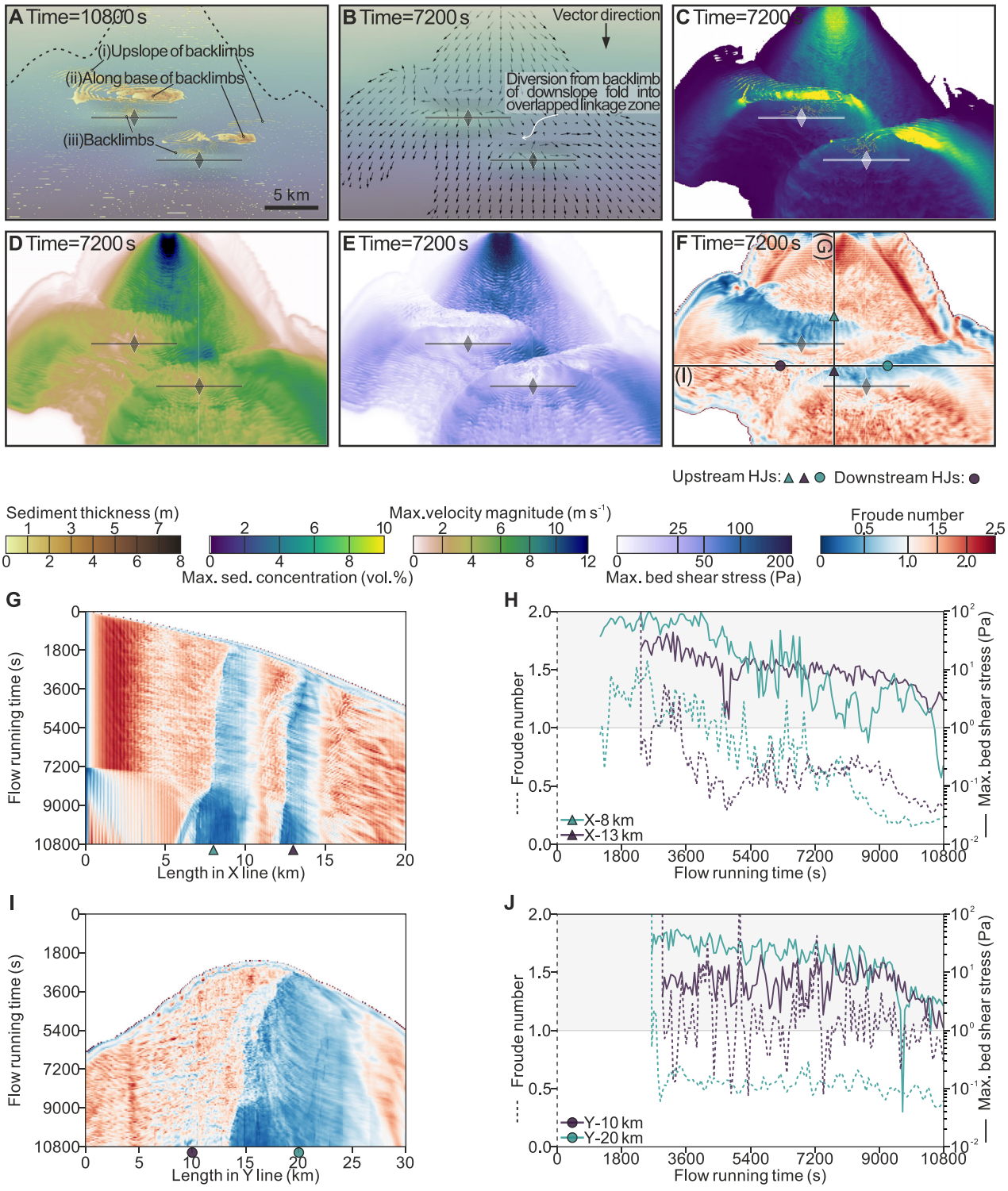

Fig. 12. Flow behaviours and sedimentary characteristics in Model 4. (A) Plan-view snapshot of sediment preferential depozones with total sand grain packing of ≥10 vol.% at 10 800 s. Note the area of accumulated sediment thickness <0.05 m is shown in white due to resolution limit and the black dashed outline indicates flow areal extent for mobile sand grain packing of ≥1 vol.%. (B) Plan-view snapshots of the flow sediment isoconcentration surface of 0.2 vol.% with mean flow velocity vectors at 7200 s. (C–F) Spatial heatmaps of the flow Maximum sediment concentration (C), Maximum velocity magnitude (D), Maximum bed shear stress (E) and Froude number (*Fr*) (F) at 7200 s. See the Video S4 for more time-series details. Note the lines of longitudinal and transverse cross-sections shown in (G) and (I). (G) Time-series plots showing *Fr* fluctuations along the longitudinal section of turbidity currents (Y-15 km). (H) In-place fluctuations of the flow *Fr* (dashed line) and Maximum bed shear stress (solid line) at position of two triangles shown in (G), which correspond to the positions of the upstream hydraulic jumps. (I) Time-series plots showing *Fr* fluctuations along the transverse section of turbidity currents (X-12.5 km). (J) In-place fluctuations of the flow *Fr* (dashed line) and Maximum bed shear stress (solid line) at position of two dots shown in (I), which correspond to the positions of the upstream and downstream hydraulic jumps. Downstream HJs, downstream hydraulic jumps; Upstream HJs, upstream hydraulic jumps.

Prather *et al.* (1998). This longitudinal deposition-bypass process integrates the 'fill-and-spill' model (Beaubouef & Friedmann, 2000; Sinclair & Tomasso, 2002) with 'tilt-and-repeat' cycles (Casagrande *et al.*, 2022). Sediment flux and volume of turbidity currents bypassing across linkage zones, fold crests and around fold tips exhibit significant variations (Table 3). The development of tortuous corridors between fold segments controls such bypass (e.g. Smith, 2004; Hay, 2012), which further enables the downslope transport of diverted flows. Consequently, turbiditic sand deposits accumulating along backlimbs of en-echelon fold segments show corresponding variations in transversal extent and thickness (Table 4). This integrated sediment dispersal pattern demonstrates that turbidity currents respond to both structural orientations, rather than being confined exclusively to either dip or transverse directions (Howlett *et al.*, 2021; Ogawa & Back, 2022; Johansson *et al.*, 2023). This study thus significantly enhances spatial prediction capabilities for sand accumulation in complex en-echelon fold systems of stepped submarine slopes.

Experiment limitations

This numerical study has certain limitations with CFD experimental assumptions that include the use of a non-erodible bedrock substrate, single flow release mode, non-cohesive sediment load, and constrained numerical grid resolution. However, consistent with previous FLOW-3D® simulations of turbidity currents (Ge *et al.*, 2017, 2018; Howlett *et al.*, 2019), these constraints do not significantly compromise the validity of our findings.

Given the limited number of models presented in this study, our research focuses exclusively on double-linkage segmented folds, while excluding triple-linkage configurations. Triple-linkage involves two synchronous or asynchronous processes of double-linkage (Bretis *et al.*, 2011; Collignon *et al.*, 2014, 2015; Fernandez & Kaus, 2014a; Nabavi & Fossen, 2021). However, the results from our double-linkage scenarios provide generic implications that can be applied to linkage evolution across multiple fold segments in evolving fold arrays. The impact of structural topography in causing diversion, reflection, blocking and funnelling of turbidity currents, as highlighted in this study, is also applicable to other structurally confined basin floors, such as rift, strike-slip and foreland-basin settings (Gawthorpe & Leeder, 2000; Patacci *et al.*, 2015; Tinterri, 2025).

The incidence angle between the turbidity currents and structural strike can range from transverse (i.e. orthogonal to structural strike) to axial (i.e. parallel to structural strike), as manifested by channel-lobe systems filling-and-spilling intraslope basins downslope and axial channel-lobe complexes infilling minibasins or on the basin floor (Oluboyo *et al.*, 2014; Howlett, 2020). Previous numerical simulations of unconfined turbidity currents have primarily examined structure-perpendicular flows across various topographies (Ge *et al.*, 2017, 2018; Howlett *et al.*, 2019). To advance this field, systematic investigations are needed to examine how incidence angles influence turbidity current hydrodynamics and sediment distribution patterns (Athmer *et al.*, 2010; Salles *et al.*, 2014; Cullen *et al.*, 2020), incorporating insights from laboratory flume-tank experiments (Soutter *et al.*, 2021; Wang *et al.*, 2025).

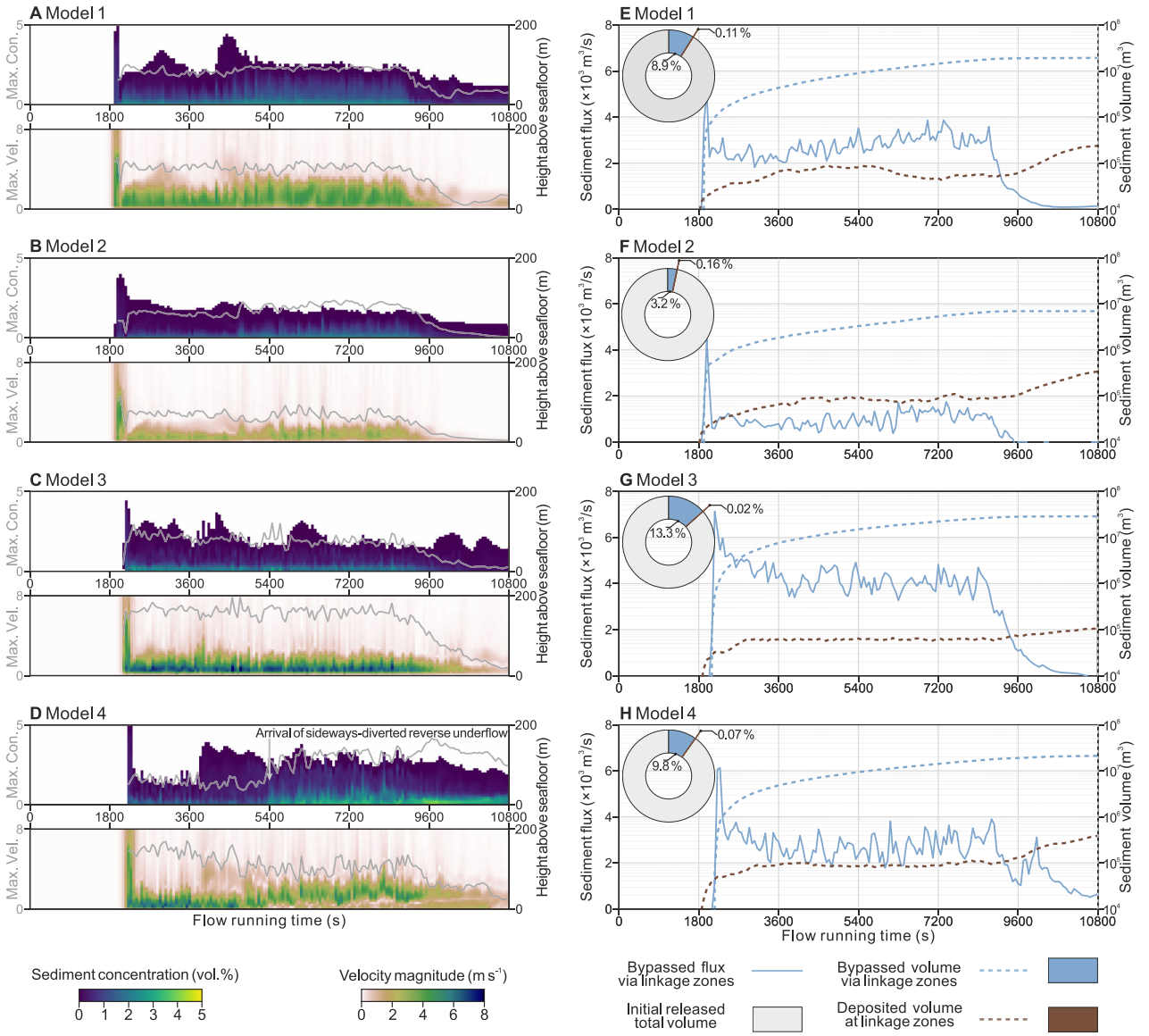

Fig. 13. Time series of hydraulic parameters at A_{mid} and temporal evolution of bypassed sediment via linkage zones during Models 1 to 4. (A–D) Time series of flow sediment concentration and velocity magnitude with grey lines for maximum values at A_{mid} in Models 1 to 4; (E–H) Fluxes (blue solid lines) and cumulative volumes of bypassed (blue dashed lines) and deposited (brown dashed lines) sediment at linkage zones in Models 1 to 4. Ring diagrams illustrate bypassed (blue) and deposited (brown) sediment volume via linkage zone as percentages of initial released total sediment volume (grey).

CONCLUSIONS

This study combines natural-scale geodynamic process modelling and CFD simulations to investigate the hydraulic behaviours and sediment dispersal patterns of unconfined turbidity currents interacting with evolving en-echelon fold segments. Two distinct types of topographically induced hydraulic jumps were observed in the upstream and downstream of the folds, respectively, when unconfined turbidity currents encountered fold topography. The upstream hydraulic jumps are followed by low-amplitude Froude number (*Fr*) fluctuations that are the result of flow deceleration and thickening caused by reverse flow with height-

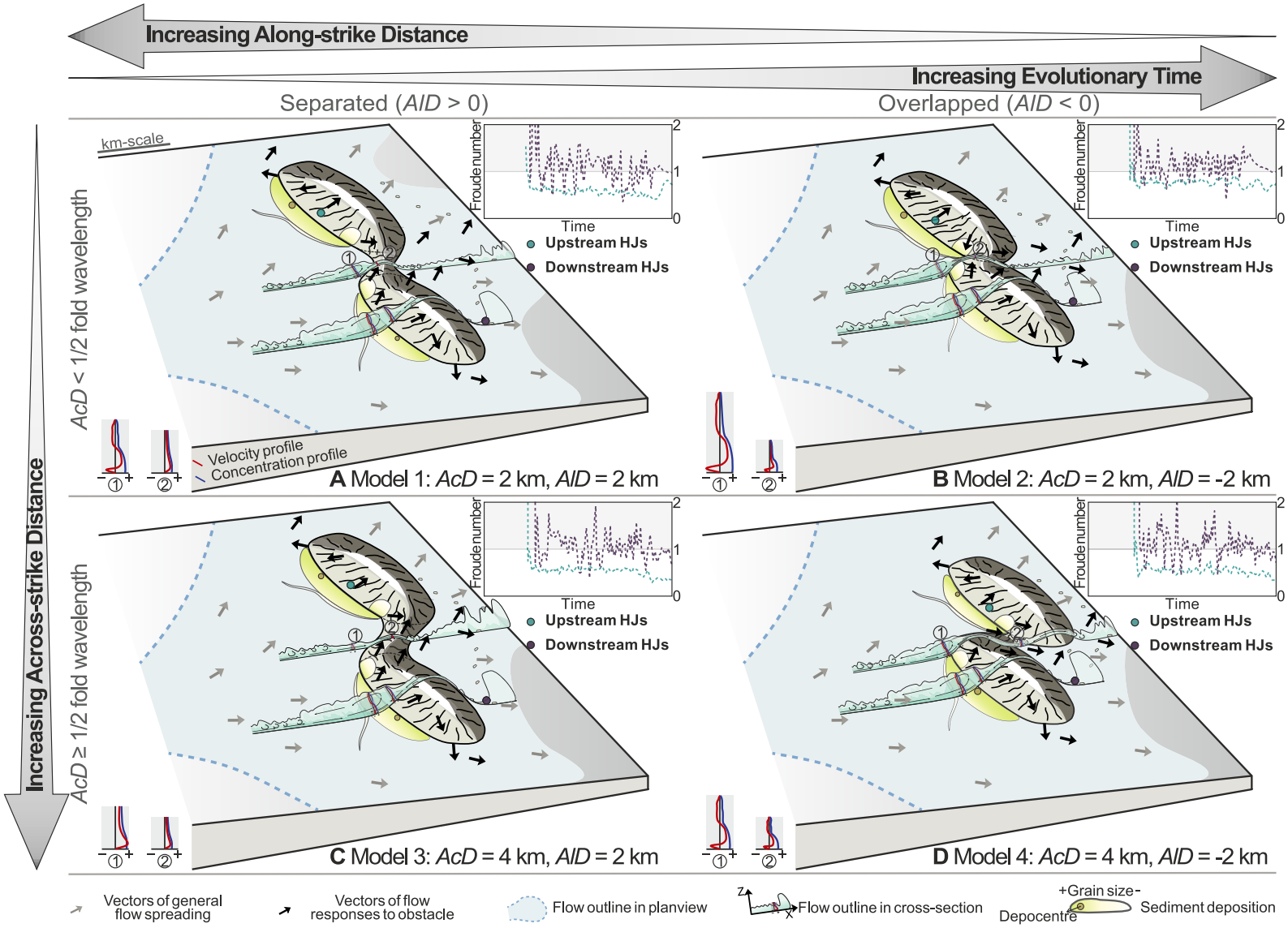

Fig. 14. Schematic diagrams summarising turbidity currents response to early-stage and late-stage en-echelon segmented folds with small (A, B) and large (C, D) *AcD*; for discussion, see text. The base maps and longitudinal cross-sections were modified from Howlett *et al.*, 2019.

suppressed Kelvin–Helmholtz (K–H) waves. Conversely, downstream hydraulic jumps exhibited high-amplitude fluctuations of *Fr* due to volumetrically small and dilute currents spilling over fold crests with enhanced large-scale K–H waves.

Sediment deposition associated with upstream hydraulic jumps occurred in three distinct depozones: (i) strike-parallel depozones upslope of backlimbs caused by upstream migration of reverse overflow bores, (ii) strike-parallel elliptical depozones along the base of fold backlimbs resulting from backward squeezing of denser near-bed suspension carried by reverse underflow and (iii) localised transverse zones on fold backlimbs associated with overspilling dilute waning flow. The upper dilute reverse overflow exhibited minimal influence on deposition, primarily functioning as a recharge mechanism for the turbidity current. In contrast to the upstream hydraulic jumps that produced confined and thick sediment deposits, downstream hydraulic jumps led to unconfined, thinner sediment accumulation along the downstream of fold forelimb, exhibiting a transition from proximal bypass to distal deposition. This mechanism explains the range of seafloor features from proximal erosional scour fields to distal depositional sediment wave fields, commonly observed downstream of slope breaks.

The impact of segmented folds on overrunning currents primarily depends upon the relief of segment boundaries, which is governed by across-strike distance (*AcD*) and the stage of linkage between adjacent folds. An early stage of linkage between en-echelon segmented folds with low linkage ratio, segment boundaries exhibit relatively low relief and serve as a zone for flow transfer and redirection. Late stages of linkage, when along-strike distance (*AlD*) between fold segments is reduced, segment boundaries remain a pathway for sediment transport across multiple folds if the across-strike distance (*AcD*) between fold segments is large. If the *AcD* is relatively small, segment boundaries have higher relief and act as an obstacle, resulting in a blocking effect similar to that of fold crest. As overlapping en-echelon folds evolve from early to late stage, sediment bypassing the folds increases, while sediment blocked by the folds decreases with reducing *AlD*. The depocentre migrates from the base of downslope fold backlimb to that of upslope fold with increasing *AcD*. Our 3D simulation results provide a flow-process based understanding for individual turbidity currents, enhancing our understanding of sedimentology and stratigraphy around fold-related topography, particularly in DWFTBs and salt- or shale-influenced basins.

ACKNOWLEDGEMENTS

The study was a part of the first author's PhD research project funded by the National Natural Science Foundation of China (grants No. 42102119 and 42472183). We also acknowledge support from the Turbidites, Topography and Tectonics (T^3) project funded by Equinor. We thank the Underworld2 development team for the open-source code used in this study (http://www.underworldcode.org). Simulation results receive support from Flow Science, Inc., developer of the computational fluid dynamics (CFD) software, FLOW-3D® (https://flow3d.com). We would also like to acknowledge the use of the cmocean (Thyng *et al.*, 2016) and scientific colormaps (Crameri *et al.*, 2020) employed in this study. We thank two reviewers, Marco Patacci and Chiara Barbieri, for comments that improve the quality of the paper. We thank associate editor Fabrizzio Felleti and editor Marc Aurell for handling the manuscript.

DATA AVAILABILITY STATEMENT

The data that support the findings of this study are available in the Supplementary material of this article.

REFERENCES

Abd El-Gawad, S., **Cantelli, A.**, **Pirmez, C.**, **Minisini, D.**, **Sylvester, Z.** and **Imran, J.** (2012a) Three-dimensional numerical simulation of turbidity currents in a submarine channel on the seafloor of The Niger Delta slope. *J. Geophys. Res. Oceans*, **117**, C05026.

Abd El-Gawad, S., **Pirmez, C.**, **Cantelli, A.**, **Minisini, D.**, **Sylvester, Z.** and **Imran, J.** (2012b) 3-D numerical simulation of turbidity currents in submarine canyons off The Niger Delta. *Mar. Geol.*, **326**, 55–66.

Alexander, J. and **Morris, S.** (1994) Observations on experimental, nonchannelized, high-concentration turbidity currents and variations in deposits around obstacles. *J. Sed. Res.*, **64**, 899–909.

Amy, L., **McCaffrey, W.** and **Kneller, B.** (2004) The influence of a lateral basin-slope on the depositional patterns of natural and experimental turbidity currents. *Geol. Soc. London Spec. Publ.*, **221**, 311–330.

Anderson, A.V., **Sickafoose, D.K.**, **Fahrer, T.R.** and **Gottschalk, R.R.** (2013) Interaction of Oligocene–Miocene deep-water depositional systems with actively evolving structures: the Lower Congo Basin, offshore Angola. In: *Tectonics and Sedimentation: implications for Petroleum Systems* (Ed Gao, D.), *AAPG Memoir*, **100**, 291–313.

Athmer, W., **Groenenberg, R.M.**, **Luthi, S.M.**, **Donselaar, M.E.**, **Sokoutis, D.** and **Willingshofer, E.** (2010) Relay ramps as pathways for turbidity currents: a study combining analogue sandbox experiments and numerical flow simulations. *Sedimentology*, **57**, 806–823.

Aydin, A. and **Schultz, R.A.** (1990) Effect of mechanical interaction on the development of strike-slip faults with echelon patterns. *J. Struct. Geol.*, **12**, 123–129.

Azpiroz-Zabala, M., **Cartigny, M.J.**, **Talling, P.J.**, **Parsons, D.R.**, **Sumner, E.J.**, **Clare, M.A.**, **Simmons, S.M.**, **Cooper, C.** and **Pope, E.L.** (2017) Newly recognized turbidity current structure can explain prolonged flushing of submarine canyons. *Sci. Adv.*, **3**, e1700200.

Bagnold, R.A. (1954) Experiments on a gravity-free dispersion of large solid spheres in a Newtonian fluid under shear. *Proc. R. Soc. Lond. Ser. A Math. Phys. Sci.*, **225**, 49–63.

Bagnold, R.A. (1962) Auto-suspension of transported sediment; turbidity currents. *Proc. R. Soc. Lond. Ser. A Math. Phys. Sci.*, **265**, 315–319.

Barton, N. and **Choubey, V.** (1977) The shear strength of rock joints in theory and practice. *Rock Mech.*, **10**, 1–54.

Basani, R., **Janocko, M.**, **Cartigny, M.J.**, **Hansen, E.W.** and **Eggenhuisen, J.T.** (2014) *MassFLOW-3D*™ as a simulation tool for turbidity currents: some preliminary results. In: *From Depositional Systems to Sedimentary Successions on the Norwegian Continental Margin* (Eds Martinius, A.W., Ravnas, R., Howell, J.A., Steel, R.J. and Wonham, J.P.), *Int. Assoc. Sed. Spec. Publ.*, **46**, 587–608.

Beaubouef, R.T. and **Friedmann, S.J.** (2000) High resolution seismic/sequence stratigraphic framework for the evolution of Pleistocene intra-slope basins, western Gulf of Mexico: depositional models and reservoir analogs. In: *Deep-Water Reservoirs of the World* (Eds Weimer, P., Slatt, R.M., Coleman, J., Rosen, N.C., Nelson, H., Bouma, A.H., Styzen, M.J. and Lawrence, D.T.), pp. 40–60. *Proceedings of the 20th Annual Research Conference*, Gulf Coast Section SEPM Foundation, Houston, Texas.

Bouchakour, M., **Zhao, X.**, **Miclău , C.** and **Yang, B.** (2023) Lateral migration and channel bend morphology around growing folds (Niger Delta continental slope). *Basin Res.*, **35**, 1154–1192.

Bretis, B., **Bartl, N.** and **Grasemann, B.** (2011) Lateral fold growth and linkage in the Zagros fold and thrust belt (Kurdistan, NE Iraq). *Basin Res.*, **23**, 615–630.

Cantero, M.I., **Shringarpure, M.** and **Balachandar, S.** (2012) Towards a universal criteria for turbulence suppression in dilute turbidity currents with non-cohesive sediments. *Geophys. Res. Lett.*, **39**, L14603.

Casagrande, J., **Hodgson, D.M.**, **Peakall, J.** and **Benac, P.M.** (2022) Fill-and-Spill, Tilt-and-Repeat (FaSTaR) cycles: stratigraphic evolution above a dynamic submarine stepped slope. *Basin Res.*, **34**, 2162–2188.

Chikita, K. (1989) A field study on turbidity currents initiated from spring runoffs. *Water Resour. Res.*, **25**, 257–271.

Clark, I.R. and **Cartwright, J.A.** (2009) Interactions between submarine channel systems and deformation in deepwater fold belts: examples from the Levant Basin, Eastern Mediterranean sea. *Mar. Petrol. Geol.*, **26**, 1465–1482.

Clark, I.R. and **Cartwright, J.A.** (2011) Key controls on submarine channel development in structurally active settings. *Mar. Petrol. Geol.*, **28**, 1333–1349.

Clark, I.R. and **Cartwright, J.A.** (2012) Interactions between coeval sedimentation and deformation from The Niger delta deepwater fold belt. In: *Application of the Principles of Seismic Geomorphology to Continental Slope and Base-of-Slope Systems: case Studies from SeaFloor and Near-Sea Floor Analogues* (Eds Prather, B.E., Deptuck, M.E., Mohrig, D., Van Hoorn, B. and Wynn, R.B.), *SEMP Spec. Publ*, **99**, 243–267.

Collignon, M., **Fernandez, N.** and **Kaus, B.** (2015) Influence of surface processes and initial topography on lateral fold growth and fold linkage mode. *Tectonics*, **34**, 1622–1645.

Collignon, M., **Kaus, B.**, **May, D.** and **Fernandez, N.** (2014) Influences of surface processes on fold growth during 3-D detachment folding. *Geochem. Geophys. Geosyst.*, **15**, 3281–3303.

Crameri, F., **Shephard, G.E.** and **Heron, P.J.** (2020) The misuse of colour in science communication. *Nat. Commun.*, **11**, 5444.

Cruz, L., **Malinski, J.**, **Hernandez, M.**, **Take, A.** and **Hilley, G.** (2011) Erosional control of the kinematics of the Aconcagua fold-and-thrust belt from numerical simulations and physical experiments. *Geology*, **39**, 439–442.

Cullen, T.M., **Collier, R.E.L.**, **Gawthorpe, R.L.**, **Hodgson, D.M.** and **Barrett, B.J.** (2020) Axial and transverse deep-water sediment supply to syn-rift fault terraces: insights from the West Xylokastro Fault Block, Gulf of Corinth, Greece. *Basin Res.*, **32**, 1105–1139.

Cumberpatch, Z.A., **Kane, I.A.**, **Soutter, E.L.**, **Hodgson, D.M.**, **Jackson, C.A.**, **Kilhams, B.A.** and **Poprawski, Y.** (2021) Interactions between deep-water gravity flows and active salt tectonics. *J. Sed. Res.*, **91**, 34–65.

Don, J., **Shaw, J.H.**, **Plesch, A.**, **Bridgwater, D.D.** and **Lufadeju, G.** (2020) Characterizing the growth of structures in three dimensions using patterns of deep-water fan and channel systems. *AAPG Bull.*, **104**, 177–203.

Doughty-Jones, G., **Lonergan, L.**, **Mayall, M.** and **Dee, S.** (2019) The role of structural growth in controlling the facies and distribution of mass transport deposits in a deep-water salt minibasin. *Mar. Petrol. Geol.*, **104**, 106–124.

Doughty-Jones, G., **Mayall, M.** and **Lonergan, L.** (2017) Stratigraphy, facies, and evolution of deep-water lobe complexes within a salt-controlled intraslope minibasin. *AAPG Bull.*, **101**, 1879–1904.

Edwards, D., **Leeder, M.**, **Best, J.** and **Pantin, H.** (1994) On experimental reflected density currents and the interpretation of certain turbidites. *Sedimentology*, **41**, 437–461.

Englert, R.G., **Vellinga, A.J.**, **Cartigny, M.J.**, **Clare, M.A.**, **Eggenhuisen, J.T.** and **Hubbard, S.M.** (2023) Controls on upstream-migrating bed forms in sandy submarine channels. *Geology*, **51**, 1137–1142.

Fernandez, N. and **Kaus, B.J.** (2014a) Fold interaction and wavelength selection in 3D models of multilayer detachment folding. *Tectonophysics*, **632**, 199–217.

Fernandez, N. and **Kaus, B.J.** (2014b) Influence of pre-existing salt diapirs on 3D folding patterns. *Tectonophysics*, **637**, 354–369.

Flow Science (2022) *FLOW-3D*® Users Manual: version 2022R1. Flow Science, Inc, Santa Fe, NM, USA.

Galy, V., **France-Lanord, C.**, **Beyssac, O.**, **Faure, P.**, **Kudrass, H.** and **Palhol, F.** (2007) Efficient organic carbon burial in

the Bengal fan sustained by the Himalayan erosional system. *Nature*, **450**, 407–410.

Gao, L., **He, C.**, **Rao, G.**, **Yang, C.-J.**, **Yuan, X.**, **Lai, J.**, **Tang, P.** and **Wu, L.** (2023) Numerical examination of the geomorphic indicators for lateral fold growth. *Geomorphology*, **432**, 108702.

Garcia, M. and **Parker, G.** (1989) Experiments on hydraulic jumps in turbidity currents near a canyon-fan transition. *Science*, **245**, 393–396.

Garcia, M.H. (1993) Hydraulic jumps in sediment-driven bottom currents. *J. Hydraul. Eng.*, **119**, 1094–1117.

Gawthorpe, R. and **Leeder, M.** (2000) Tectono-sedimentary evolution of active extensional basins. *Basin Res.*, **12**, 195–218.

Ge, Z., **Nemec, W.**, **Gawthorpe, R.L.** and **Hansen, E.W.** (2017) Response of unconfined turbidity current to normal-fault topography. *Sedimentology*, **64**, 932–959.

Ge, Z., **Nemec, W.**, **Gawthorpe, R.L.**, **Rotevatn, A.** and **Hansen, E.W.** (2018) Response of unconfined turbidity current to relay-ramp topography: insights from process-based numerical modelling. *Basin Res.*, **30**, 321–343.

Ge, Z., **Nemec, W.**, **Vellinga, A.J.** and **Gawthorpe, R.L.** (2022) How is a turbidite actually deposited? *Sci. Adv.*, **8**, eabl9124.

Gee, M. and **Gawthorpe, R.** (2006) Submarine channels controlled by salt tectonics: examples from 3D seismic data offshore Angola. *Mar. Petrol. Geol.*, **23**, 443–458.

Gee, M., **Gawthorpe, R.L.**, **Bakke, K.** and **Friedmann, S.** (2007) Seismic geomorphology and evolution of submarine channels from the Angolan continental margin. *J. Sed. Res.*, **77**, 433–446.

Gee, M.J., **Masson, D.G.**, **Watts, A.B.** and **Mitchell, N.C.** (2001) Passage of debris flows and turbidity currents through a topographic constriction: seafloor erosion and diversion of flow pathways. *Sedimentology*, **48**, 1389–1409.

Grasemann, B. and **Schmalholz, S.M.** (2012) Lateral fold growth and fold linkage. *Geology*, **40**, 1039–1042.

Grujić, D. (1993) The influence of initial fold geometry on Type 1 and Type 2 interference patterns: an experimental approach. *J. Struct. Geol.*, **15**, 293–307.

Hay, D.C. (2012) Stratigraphic evolution of a tortuous corridor from the stepped slope of Angola. In: *Application of the Principles of Seismic Geomorphology to Continental Slope and Base-of-Slope Systems: case Studies from SeaFloor and Near-Sea Floor Analogues* (Eds Prather, B.E., Deptuck, M.E., Mohrig, D., Van Hoorn, B. and Wynn, R.B.), *SEMP Spec. Publ*, **99**, 163–180.

Heijnen, M., **Mienis, F.**, **Gates, A.**, **Bett, B.**, **Hall, R.**, **Hunt, J.**, **Kane, I.**, **Pebody, C.**, **Huvenne, V.** and **Soutter, E.** (2022) Challenging the highstand-dormant paradigm for land-detached submarine canyons. *Nat. Commun.*, **13**, 3448.

Heimsund, S., **Xu, J.** and **Nemec, W.** (2007) Numerical simulation of recent turbidity currents in the Monterey Canyon system, offshore California. AGU Fall Meeting Abstracts, Pt.1, 996.

Heiniö, P. and **Davies, R.J.** (2006) Degradation of compressional fold belts: deep-water Niger Delta. *AAPG Bull.*, **90**, 753–770.

Heiniö, P. and **Davies, R.J.** (2007) Knickpoint migration in submarine channels in response to fold growth, western Niger Delta. *Mar. Petrol. Geol.*, **24**, 434–449.

Hesse, S., **Back, S.** and **Franke, D.** (2009) The deep-water fold-and-thrust belt offshore NW Borneo: gravity-driven versus basement-driven shortening. *Geol. Soc. Am. Bull.*, **121**, 939–953.

Hesse, S., **Back, S.** and **Franke, D.** (2010) The structural evolution of folds in a deepwater fold and thrust belt–a case study from the Sabah continental margin offshore NW Borneo, SE Asia. *Mar. Petrol. Geol.*, **27**, 442–454.

Higgins, S., **Davies, R.J.** and **Clarke, B.** (2007) Antithetic fault linkages in a deep water fold and thrust belt. *J. Struct. Geol.*, **29**, 1900–1914.

Hodgson, D.M., **Peakall, J.** and **Maier, K.L.** (2022) Submarine channel mouth settings: processes, geomorphology, and deposits. *Front. Earth Sci.*, **10**, 790320.

Howarth, J.D., **Orpin, A.R.**, **Kaneko, Y.**, **Strachan, L.J.**, **Nodder, S.D.**, **Mountjoy, J.J.**, **Barnes, P.M.**, **Bostock, H.C.**, **Holden, C.** and **Jones, K.** (2021) Calibrating the marine turbidite palaeoseismometer using the 2016 Kaikōura earthquake. *Nat. Geosci.*, **14**, 161–167.

Howlett, D.M., **Gawthorpe, R.L.**, **Ge, Z.**, **Rotevatn, A.** and **Jackson, C.A.L.** (2021) Turbidites, topography and tectonics: evolution of submarine channel-lobe systems in the salt-influenced Kwanza Basin, offshore Angola. *Basin Res.*, **33**, 1076–1110.

Howlett, D.M., **Ge, Z.**, **Nemec, W.**, **Gawthorpe, R.L.**, **Rotevatn, A.** and **Jackson, C.A.L.** (2019) Response of unconfined turbidity current to deep-water fold and thrust belt topography: orthogonal incidence on solitary and segmented folds. *Sedimentology*, **66**, 2425–2454.

Howlett, D.M. (2020) *Response of deep-water depositional systems to salt-influenced topography: Miocene, offshore Angola*. PhD thesis, University of Bergen, Bergen, Norway.

Huang, H., **Imran, J.** and **Pirmez, C.** (2007) Numerical modeling of poorly sorted depositional turbidity currents. *J. Geophys. Res. Oceans*, **112**, C01014.

Huang, H., **Imran, J.** and **Pirmez, C.** (2012) The depositional characteristics of turbidity currents in submarine sinuous channels. *Mar. Geol.*, **329**, 93–102.

Hughes Clarke, J.E. (2016) First wide-angle view of channelized turbidity currents links migrating cyclic steps to flow characteristics. *Nat. Commun.*, **7**, 11896.

Huismans, R. and **Beaumont, C.** (2011) Depth-dependent extension, two-stage breakup and cratonic underplating at rifted margins. *Nature*, **473**, 74–78.

Jackson, M.P. and **Hudec, M.R.** (2017) *Salt Tectonics: principles and Practice*. Cambridge University Press, Cambridge, UK, 495 p.

Jackson, M.P. and **Talbot, C.J.** (1986) External shapes, strain rates, and dynamics of salt structures. *Geol. Soc. Am. Bull.*, **97**, 305–323.

Janocko, M., **Cartigny, M.**, **Nemec, W.** and **Hansen, E.** (2013) Turbidity current hydraulics and sediment deposition in erodible sinuous channels: laboratory experiments and numerical simulations. *Mar. Petrol. Geol.*, **41**, 222–249.

Johansson, M., **van Doorn, J.** and **Stow, D.** (2023) Geomorphology of Deep Marine Sediments, Northwest Borneo. *Proceedings of the 2023 Southeast Asia Petroleum Exploration Society (SEAPEX) Conference, 2023*, 22.

Johns, M. and **Mosher, S.** (1996) Physical models of regional fold superposition: the role of competence contrast. *J. Struct. Geol.*, **18**, 475–492.

Jolly, B.A., **Lonergan, L.** and **Whittaker, A.C.** (2016) Growth history of fault-related folds and interaction with seabed channels in the toe-thrust region of the deep-water Niger delta. *Mar. Petrol. Geol.*, **70**, 58–76.

Jolly, B.A., **Whittaker, A.C.** and **Lonergan, L.** (2017) Quantifying the geomorphic response of modern submarine channels to actively growing folds and thrusts, deep-water Niger Delta. *GSA Bull.*, **129**, 1123–1139.

Kane, I.A., **Clare, M.A.**, **Miramontes, E.**, **Wogelius, R.**, **Rothwell, J.J.**, **Garreau, P.** and **Pohl, F.** (2020) Seafloor microplastic hotspots controlled by deep-sea circulation. *Science*, **368**, 1140–1145.

Keavney, E., **Peakall, J.**, **Wang, R.**, **Hodgson, D.M.**, **Kane, I.A.**, **Keevil, G.M.**, **Brown, H.C.**, **Clare, M.A.** and **Hughes, M.J.** (2025) Unconfined gravity current interactions with orthogonal topography: implications for combined-flow processes and the depositional record. *Sedimentology*, **72**, 67–99.

Kessel, T.V. and **Kranenburg, C.** (1996) Gravity current of fluid mud on sloping bed. *J. Hydraul. Eng.*, **122**, 710–717.

Kneller, B. (1995) Beyond the turbidite paradigm: physical models for deposition of turbidites and their implications for reservoir prediction. In: *Characterisation of Deep Marine Clastic Systems* (Eds Hartley, A. and Prosser, D.J.), *Geological Society, London, Special Publications*, **94**, 31–49.

Kneller, B., **Edwards, D.**, **McCaffrey, W.** and **Moore, R.** (1991) Oblique reflection of turbidity currents. *Geology*, **19**, 250–252.

Kneller, B. and **McCaffrey, B.** (1995) Modelling the effects of salt-induced topography on deposition from turbidity currents. In: *Salt, sediments and hydrocarbon* (Eds Travis, C., Harrison, H., Hudec, M., Vendeville, B., Peel, F. and Perkins, B.), *SEPM Spec. Publ*, **16**, 137–145.

Kneller, B. and **McCaffrey, W.** (1999) Depositional effects of flow nonuniformity and stratification within turbidity currents approaching a bounding slope; diversion, reflection, and facies variation. *J. Sed. Res.*, **69**, 980–991.

Kneller, B.C. and **Branney, M.J.** (1995) Sustained high-density turbidity currents and the deposition of thick massive sands. *Sedimentology*, **42**, 607–616.

Komar, P.D. (1971) Hydraulic jumps in turbidity currents. *Geol. Soc. Am. Bull.*, **82**, 1477–1488.

Kuenen, P.H. (1966) Matrix of turbidites: experimental approach. *Sedimentology*, **7**, 267–297.

Lamb, M.P., **Toniolo, H.** and **Parker, G.** (2006) Trapping of sustained turbidity currents by intraslope minibasins. *Sedimentology*, **53**, 147–160.

Lewis, K. (1971) Slumping on a continental slope inclined at 1°–4°. *Sedimentology*, **16**, 97–110.

Liu, M., **Wang, Z.**, **Yu, K.** and **Xu, J.** (2023) Two distinct types of turbidity currents observed in the Manila Trench, South China Sea. *Commun. Earth Environ.*, **4**, 108.

Long, J.J. and **Imber, J.** (2011) Geological controls on fault relay zone scaling. *J. Struct. Geol.*, **33**, 1790–1800.

MacDonald, R.G., **Alexander, J.**, **Bacon, J.C.** and **Cooker, M.J.** (2009) Flow patterns, sedimentation and deposit architecture under a hydraulic jump on a non-eroding bed: defining hydraulic-jump unit bars. *Sedimentology*, **56**, 1346–1367.

Manger, G.E. (1963) Porosity and bulk density of sedimentary rocks. USGS Bulletin 1144.

Maselli, V., **Micallef, A.**, **Normandeau, A.**, **Oppo, D.**, **Iacopini, D.**, **Green, A.** and **Ge, Z.** (2021) Active faulting controls bedform development on a deep-water fan. *Geology*, **49**, 1495–1500.

Mastbergen, D.R. and **Van Den Berg, J.H.** (2003) Breaching in fine sands and the generation of sustained turbidity currents in submarine canyons. *Sedimentology*, **50**, 625–637.

Mayall, M., **Lonergan, L.**, **Bowman, A.**, **James, S.**, **Mills, K.**, **Primmer, T.**, **Pope, D.**, **Rogers, L.** and **Skeene, R.** (2010) The response of turbidite slope channels to growth-induced seabed topography. *AAPG Bull.*, **94**, 1011–1030.

McArthur, A.D., **Crisóstomo-Figueroa, A.**, **Wunderlich, A.**, **Karvelas, A.** and **McCaffrey, W.D.** (2022) Sedimentation on structurally complex slopes: neogene to recent deep-water sedimentation patterns across the central Hikurangi subduction margin, New Zealand. *Basin Res.*, **34**, 1807–1837.

Meiburg, E. and **Kneller, B.** (2010) Turbidity currents and their deposits. *Annu. Rev. Fluid Mech.*, **42**, 135–156.

Meiburg, E., **Radhakrishnan, S.** and **Nasr-Azadani, M.** (2015) Modeling gravity and turbidity currents: computational approaches and challenges. *Appl. Mech. Rev.*, **67**, 40802.

Meyer-Peter, E. and **Müller, R.** (1948) Formulas for bed-load transport. In: *IAHSR 2nd meeting, Stockholm, Appendix 2*. IAHR, Madrid, Spain.

Middleton, G.V. (1976) Subaqueous sediment transport and deposition by sediment gravity flows. In: *Marine Sediment Transport and Environmental Management* (Eds Stanley, D.J. and Swift, D.J.P.), pp. 197–218. Wiley, New York.

Middleton, G.V. (1993) Sediment deposition from turbidity currents. *Annu. Rev. Earth Planet. Sci.*, **21**, 89–114.

Mitchell, W.H., **Whittaker, A.C.**, **Mayall, M.** and **Lonergan, L.** (2021a) New models for submarine channel deposits on structurally complex slopes: examples from The Niger Delta system. *Mar. Petrol. Geol.*, **129**, 105040.

Mitchell, W.H., **Whittaker, A.C.**, **Mayall, M.**, **Lonergan, L.** and **Pizzi, M.** (2021b) Quantifying the relationship between structural deformation and the morphology of submarine channels on The Niger Delta continental slope. *Basin Res.*, **33**, 186–209.

Mitchell, W.H., **Whittaker, A.C.**, **Mayall, M.**, **Lonergan, L.** and **Pizzi, M.** (2022) Quantifying structural controls on submarine channel architecture and kinematics. *GSA Bull.*, **134**, 928–940.

Mondy, L.S., **Rey, P.F.** and **Duclaux, G.** (2023) The role of surface processes in basin inversion and breakup unconformity. *Geology*, **51**, 220–224.

Moresi, L., **Betts, P.G.**, **Miller, M.S.** and **Cayley, R.A.** (2014) Dynamics of continental accretion. *Nature*, **508**, 245–248.

Moresi, L., **Dufour, F.** and **Mühlhaus, H.-B.** (2003) A Lagrangian integration point finite element method for large deformation modeling of viscoelastic geomaterials. *J. Comput. Phys.*, **184**, 476–497.

Moresi, L., **Mühlhaus, H.-B.**, **Lemiale, V.** and **May, D.** (2007) Incompressible viscous formulations for deformation and yielding of the lithosphere. *Geol. Soc. London Spec. Publ.*, **282**, 457–472.

Morley, C., **King, R.**, **Hillis, R.**, **Tingay, M.** and **Backe, G.** (2011) Deepwater fold and thrust belt classification, tectonics, structure and hydrocarbon prospectivity: a review. *Earth-Sci. Rev.*, **104**, 41–91.

Morley, C. and **Leong, L.C.** (2008) Evolution of deep-water synkinematic sedimentation in a piggyback basin, determined from three-dimensional seismic reflection data. *Geosphere*, **4**, 939–962.

Morley, C.K. (2009) Growth of folds in a deep-water setting. *Geosphere*, **5**, 59–89.

Morris, S.A. and **Alexander, J.** (2003) Changes in flow direction at a point caused by obstacles during passage of a density current. *J. Sed. Res.*, **73**, 621–629.

Muck, M.T. and **Underwood, M.B.** (1990) Upslope flow of turbidity currents: a comparison among field observations, theory, and laboratory models. *Geology*, **18**, 54–57.

Mulder, T., **Syvitski, J.P.**, **Migeon, S.**, **Faugères, J.-C.** and **Savoye, B.** (2003) Marine hyperpycnal flows: initiation, behavior and related deposits. A review. *Mar. Petrol. Geol.*, **20**, 861–882.

Mulder, T., **Syvitski, J.P.** and **Skene, K.I.** (1998) Modeling of erosion and deposition by turbidity currents generated at river mouths. *J. Sed. Res.*, **68**, 124–137.

Muñoz-Royo, C., **Ouillon, R.**, **El Mousadik, S.**, **Alford, M.H.** and **Peacock, T.** (2022) An in situ study of abyssal turbidity-current sediment plumes generated by a deep seabed polymetallic nodule mining preprototype collector vehicle. *Sci. Adv.*, **8**, eabn1219.

Nabavi, S.T. and **Fossen, H.** (2021) Fold geometry and folding–a review. *Earth-Sci. Rev.*, **222**, 103812.

Ogawa, K. and **Back, S.** (2022) Seismostratigraphic and sedimentological characterization of deepwater channel systems on the NW Borneo margin: sediment sources and structurally-controlled routing system. *J. Asian Earth Sci.*, **232**, 105126.

Oluboyo, A., **Gawthorpe, R.**, **Bakke, K.** and **Hadler-Jacobsen, F.** (2014) Salt tectonic controls on deep-water turbidite depositional systems: Miocene, southwestern Lower Congo Basin, offshore Angola. *Basin Res.*, **26**, 597–620.

Oveisi, B., **Lavé, J.** and **van der Beek, P.** (2007) Rates and processes of active folding evidenced by Pleistocene terraces at the central Zagros front (Iran). In: *Thrust Belts and Foreland Basins: from Fold Kinematics to Hydrocarbon Systems* (Eds Lacombe, O., Roure, F., Lavé, J. and Vergés, J.), pp. 267–287. Springer, Berlin, Heidelberg.

Pantin, H. and **Leeder, M.** (1987) Reverse flow in turbidity currents: the role of internal solitons. *Sedimentology*, **34**, 1143–1155.

Patacci, M., **Haughton, P.D.** and **McCaffrey, W.D.** (2015) Flow behavior of ponded turbidity currents. *J. Sed. Res.*, **85**, 885–902.

Paull, C.K., **Talling, P.J.**, **Maier, K.L.**, **Parsons, D.**, **Xu, J.**, **Caress, D.W.**, **Gwiazda, R.**, **Lundsten, E.M.**, **Anderson, K.** and **Barry, J.P.** (2018) Powerful turbidity currents driven by dense basal layers. *Nat. Commun.*, **9**, 4114.

Piper, D.J., **Cochonat, P.** and **Morrison, M.L.** (1999) The sequence of events around the epicentre of the 1929 Grand Banks earthquake: initiation of debris flows and turbidity current inferred from sidescan sonar. *Sedimentology*, **46**, 79–97.

Piper, D.J. and **Normark, W.R.** (2009) Processes that initiate turbidity currents and their influence on turbidites: a marine geology perspective. *J. Sed. Res.*, **79**, 347–362.

Pizzi, M., **Lonergan, L.**, **Whittaker, A.C.** and **Mayall, M.** (2020) Growth of a thrust fault array in space and time: an example from the deep-water Niger delta. *J. Struct. Geol.*, **137**, 104088.

Pizzi, M., **Whittaker, A.C.**, **Mayall, M.** and **Lonergan, L.** (2023) Structural controls on the pathways and sedimentary architecture of submarine channels: new constraints from The Niger Delta. *Basin Res.*, **35**, 141–171.

Pohl, F., **Eggenhuisen, J.T.**, **Tilston, M.** and **Cartigny, M.** (2019) New flow relaxation mechanism explains scour fields at the end of submarine channels. *Nat. Commun.*, **10**, 4425.

Pope, E.L., **Cartigny, M.J.**, **Clare, M.A.**, **Talling, P.J.**, **Lintern, D.G.**, **Vellinga, A.**, **Hage, S.**, **Açikalin, S.**, **Bailey, L.** and **Chapplow, N.** (2022b) First source-to-sink monitoring shows dense head controls sediment flux and runout in turbidity currents. *Sci. Adv.*, **8**, eabj3220.

Pope, E.L., **Heijnen, M.S.**, **Talling, P.J.**, **Jacinto, R.S.**, **Gaillot, A.**, **Baker, M.L.**, **Hage, S.**, **Hasenhündl, M.**, **Heerema, C.J.** and **McGhee, C.** (2022a) Carbon and sediment fluxes inhibited in the submarine Congo Canyon by landslide-damming. *Nat. Geosci.*, **15**, 845–853.

Prather, B.E., **Booth, J.R.**, **Steffens, G.S.** and **Craig, P.A.** (1998) Classification, lithologic calibration, and stratigraphic succession of seismic facies of intraslope basins, deep-water Gulf of Mexico. *AAPG Bull.*, **82**, 701–728.

Ramsey, L.A., **Walker, R.T.** and **Jackson, J.** (2008) Fold evolution and drainage development in the Zagros mountains of Fars province, SE Iran. *Basin Res.*, **20**, 23–48.

Ravnås, R. and **Steel, R.J.** (1998) Architecture of marine rift-basin successions. *AAPG Bull.*, **82**, 110–146.

Richardson, J. and **Zaki, W.** (1954) The sedimentation of a suspension of uniform spheres under conditions of viscous flow. *Chem. Eng. Sci.*, **3**, 65–73.

Rottman, J.W. and **Simpson, J.E.** (1989) The formation of internal bores in the atmosphere: a laboratory model. *Q. J. R. Meteorol. Soc.*, **115**, 941–963.

Salinas, J., **Balachandar, S.**, **Shringarpure, M.**, **Fedele, J.**, **Hoyal, D.** and **Cantero, M.** (2020) Soft transition between subcritical and supercritical currents through intermittent cascading interfacial instabilities. *Proc. Natl. Acad. Sci. USA*, **117**, 18278–18284.

Salinas, J.S., **Balachandar, S.**, **Shringarpure, M.**, **Fedele, J.**, **Hoyal, D.**, **Zuñiga, S.** and **Cantero, M.I.** (2021) Anatomy of subcritical submarine flows with a lutocline and an intermediate destruction layer. *Nat. Commun.*, **12**, 1649.

Salles, L., **Ford, M.** and **Joseph, P.** (2014) Characteristics of axially-sourced turbidite sedimentation on an active wedge-top basin (Annot Sandstone, SE France). *Mar. Petrol. Geol.*, **56**, 305–323.

Schmalholz, S.M. (2008) 3D numerical modeling of forward folding and reverse unfolding of a viscous single-layer: implications for the formation of folds and fold patterns. *Tectonophysics*, **446**, 31–41.

Schmid, D., **Dabrowski, M.** and **Krotkiewski, M.** (2008) Evolution of large amplitude 3D fold patterns: a FEM study. *Phys. Earth Planet. Inter.*, **171**, 400–408.

Simons, W., **Socquet, A.**, **Vigny, C.**, **Ambrosius, B.**, **Haji Abu, S.**, **Promthong, C.**, **Subarya, C.**, **Sarsito, D.**, **Matheussen, S.** and **Morgan, P.** (2007) A decade of GPS in Southeast Asia: resolving Sundaland motion and boundaries. *J. Geophys. Res. Solid Earth*, **112**, B06420.

Simpson, J.E. (1986) Mixing at the front of a gravity current. *Acta Mech.*, **63**, 245–253.

Sinclair, H. and **Tomasso, M.** (2002) Depositional evolution of confined turbidite basins. *J. Sed. Res.*, **72**, 451–456.

Slootman, A. and **Cartigny, M.J.** (2020) Cyclic steps: review and aggradation-based classification. *Earth-Sci. Rev.*, **201**, 102949.

Smith, G., **Rowley, P.**, **Williams, R.**, **Giordano, G.**, **Trolese, M.**, **Silleni, A.**, **Parsons, D.R.** and **Capon, S.** (2020) A bedform phase diagram for dense granular currents. *Nat. Commun.*, **11**, 2873.

Smith, R. (2004) Silled sub-basins to connected tortuous corridors: sediment distribution systems on topographically complex sub-aqueous slopes. *Geol. Soc. London Spec. Publ.*, **222**, 23–43.

Song, G., **Wang, M.**, **Jiang, D.**, **Chen, Z.**, **Yan, B.** and **Feng, W.** (2021) Along-strike structural linkage and interaction in an active thrust fault system: a case study from the

western Sichuan foreland basin, China. *Basin Res.*, **33**, 210–226.

Soulsby, R. (1997) 9. Bedload transport. In: *Dynamics of Marine Sands* (Ed Soulsby, R.), pp. 155–170. Thomas Telford Publications, London.

Soutter, E.L., **Bell, D.**, **Cumberpatch, Z.A.**, **Ferguson, R.A.**, **Spychala, Y.T.**, **Kane, I.A.** and **Eggenhuisen, J.T.** (2021) The influence of confining topography orientation on experimental turbidity currents and geological implications. *Front. Earth Sci.*, **8**, 540633.

Sumner, E., **Peakall, J.**, **Parsons, D.**, **Wynn, R.**, **Darby, S.**, **Dorrell, R.**, **McPhail, S.**, **Perrett, J.**, **Webb, A.** and **White, D.** (2013) First direct measurements of hydraulic jumps in an active submarine density current. *Geophys. Res. Lett.*, **40**, 5904–5908.

Talling, P.J., **Baker, M.L.**, **Pope, E.L.**, **Ruffell, S.C.**, **Jacinto, R.S.**, **Heijnen, M.S.**, **Hage, S.**, **Simmons, S.M.**, **Hasenhündl, M.** and **Heerema, C.J.** (2022) Longest sediment flows yet measured show how major rivers connect efficiently to deep sea. *Nat. Commun.*, **13**, 4193.

Talling, P.J., **Cartigny, M.J.**, **Pope, E.**, **Baker, M.**, **Clare, M.A.**, **Heijnen, M.**, **Hage, S.**, **Parsons, D.R.**, **Simmons, S.M.** and **Paull, C.K.** (2023) Detailed monitoring reveals the nature of submarine turbidity currents. *Nat. Rev. Earth Environ.*, **9**, 1–17.

Talling, P.J., **Masson, D.G.**, **Sumner, E.J.** and **Malgesini, G.** (2012) Subaqueous sediment density flows: depositional processes and deposit types. *Sedimentology*, **59**, 1937–2003.

Talling, P.J., **Paull, C.K.** and **Piper, D.J.** (2013) How are subaqueous sediment density flows triggered, what is their internal structure and how does it evolve? Direct observations from monitoring of active flows. *Earth-Sci. Rev.*, **125**, 244–287.

Thyng, K.M., **Greene, C.A.**, **Hetland, R.D.**, **Zimmerle, H.M.** and **DiMarco, S.F.** (2016) True colors of oceanography: guidelines for effective and accurate colormap selection. *Oceanography*, **29**, 9–13.

Tinterri, R. (2025) A new turbidite facies-tract scheme including supercritical and transitional sand–mud flows: an outcrop perspective from Mediterranean-type foreland basins. *J. Sed. Res.*, **95**, 239–272.

Tinterri, R., **Magalhaes, P.M.**, **Tagliaferri, A.** and **Cunha, R.** (2016) Convolute laminations and load structures in turbidites as indicators of flow reflections and decelerations against bounding slopes. Examples from the Marnoso-arenacea Formation (northern Italy) and Annot Sandstones (south eastern France). *Sed. Geol.*, **344**, 382–407.

Tinterri, R., **Mazza, T.** and **Magalhaes, P.M.** (2022) Contained-reflected megaturbidites of the Marnoso-arenacea Formation (Contessa key bed) and helminthoid flysches (northern Apennines, Italy) and Hecho Group (south-western Pyrenees). *Front. Earth Sci.*, **10**, 817012.

Tinterri, R. and **Piazza, A.** (2019) Turbidites facies response to the morphological confinement of a foredeep (Cervarola Sandstones Formation, Miocene, northern Apennines, Italy). *Sedimentology*, **66**, 636–674.

Tinterri, R. and **Tagliaferri, A.** (2015) The syntectonic evolution of foredeep turbidites related to basin segmentation: facies response to the increase in tectonic confinement (Marnoso-arenacea Formation, Miocene, Northern Apennines, Italy). *Mar. Petrol. Geol.*, **67**, 81–110.

Vellinga, A.J., **Cartigny, M.J.**, **Eggenhuisen, J.T.** and **Hansen, E.W.** (2018) Morphodynamics and depositional signature of low-aggradation cyclic steps: new insights from a depth-resolved numerical model. *Sedimentology*, **65**, 540–560.

Wahab, A., **Hoyal, D.C.**, **Shringarpure, M.** and **Straub, K.M.** (2022) A dimensionless framework for predicting submarine fan morphology. *Nat. Commun.*, **13**, 7563.

Wang, R., **Peakall, J.**, **Hodgson, D.M.**, **Keavney, E.**, **Brown, H.C.** and **Keevil, G.M.** (2025) Three-dimensional gravity current interactions with oblique slopes: deflection, reflection and combined-flow behaviours. *Sedimentology*, **72**, 2121–2159.

Weijermars, R., **Jackson, M.P.A.** and **Vendeville, B.C.** (1993) Rheological and tectonic modeling of salt provinces. *Tectonophysics*, **217**, 143–174.

Wells, M.G. and **Dorrell, R.M.** (2021) Turbulence processes within turbidity currents. *Annu. Rev. Fluid Mech.*, **53**, 59–83.

Wu, J., **McClay, K.** and **de Vera, J.** (2020) Growth of triangle zone fold-thrusts within the NW Borneo deep-water fold belt, offshore Sabah, southern South China Sea. *Geosphere*, **16**, 329–356.

Wynn, R.B., **Kenyon, N.H.**, **Masson, D.G.**, **Stow, D.A.** and **Weaver, P.P.** (2002) Characterization and recognition of deep-water channel-lobe transition zones. *AAPG Bull.*, **86**, 1441–1462.

Xu, J., **Noble, M.** and **Rosenfeld, L.K.** (2004) In-situ measurements of velocity structure within turbidity currents. *Geophys. Res. Lett.*, **31**, L09311.

Yakhot, V., **Orszag, S.**, **Thangam, S.**, **Gatski, T.** and **Speziale, C.** (1992) Development of turbulence models for shear flows by a double expansion technique. *Physics of Fluids A: Fluid Dynamics*, **4**, 1510–1520.

Zavala, C., **Ponce, J.J.**, **Arcuri, M.**, **Drittanti, D.**, **Freije, H.** and **Asensio, M.** (2006) Ancient lacustrine hyperpycnites: a depositional model from a case study in the Rayoso Formation (Cretaceous) of west-central Argentina. *J. Sed. Res.*, **76**, 41–59.

Zhang, L., **Yang, X.**, **Huang, W.**, **Yang, H.** and **Li, S.** (2021) Fold segment linkage and lateral propagation along the Qiulitage anticline, South Tianshan, NW China. *Geomorphology*, **381**, 107662.

Zhang, Y., **Liu, Z.**, **Zhao, Y.**, **Colin, C.**, **Zhang, X.**, **Wang, M.**, **Zhao, S.** and **Kneller, B.** (2018) Long-term in situ observations on typhoon-triggered turbidity currents in the deep sea. *Geology*, **46**, 675–678.

Manuscript received 13 August 2025; revision accepted 17 January 2026

Supporting Information

Additional information may be found in the online version of this article:

Video S1. This animation depicts the three-dimensional flow sediment isoconcentration surface of 0.2 vol.% (coloured by X velocity) and spatial heatmaps of key hydraulic parameters recorded per minute in Model 1 ($AcD = 2$ km, $AlD = 2$ km). The visualised parameters include: Maximum sediment concentration, maximum velocity magnitude, maximum bed shear stress, and Froude number.

Video S2. This animation depicts the three-dimensional flow sediment isoconcentration surface of 0.2 vol.% (coloured by X velocity) and spatial heatmaps of key hydraulic parameters recorded per minute in Model 2 ($AcD = 2$ km, $AlD = -2$ km). The visualised parameters include: Maximum sediment concentration, maximum velocity magnitude, maximum bed shear stress, and Froude number.

Video S3. This animation depicts the three-dimensional flow sediment isoconcentration surface of 0.2 vol.% (coloured by X velocity) and spatial heatmaps of key hydraulic parameters recorded per minute in Model 3 ($AcD = 4$ km, $AlD = 2$ km). The visualised parameters include: Maximum sediment concentration, maximum velocity magnitude, maximum bed shear stress, and Froude number.

Video S4. This animation depicts the three-dimensional flow sediment isoconcentration surface of 0.2 vol.% (coloured by X velocity) and spatial heatmaps of key hydraulic parameters recorded per minute in Model 4 ($AcD = 4$ km, $AlD = -2$ km). The visualised parameters include: Maximum sediment concentration, maximum velocity magnitude, maximum bed shear stress, and Froude number.

Table S1. Maximum, average, and standard deviation of preferential deposited sediment thicknesses (sand grain packing of ≥10 vol.%) in Models 1 to 4.